ON THE DETECTION OF EXOMOONS

Michael Hippke
Institute for Data Analysis, Luiter Straße 21b, 47506 Neukirchen-Vluyn, Germany

ABSTRACT

Despite the discovery of thousands of exoplanets, no exomoons have been detected so far. We test a recently developed method for exomoon search, the *orbital sampling effect* (OSE), using the full exoplanet photometry from the *Kepler* Space Telescope. The OSE is applied to phase-folded transits, for which we present a framework to detect false positives, and discuss four candidates which pass several of our tests. Using numerical simulations, we inject exomoon signals into real *Kepler* data and retrieve them, showing that under favorable conditions, exomoons can be found with *Kepler* and the OSE method. In addition, we super-stack a large sample of *Kepler* planets to search for the average exomoon OSE and the accompanying increase in noise, the *scatter peak*. We find significant exomoon presence for planets with $35d < P < 80d$, with an average dip per planet of 6 ± 2ppm, about the radius of Ganymede.

Subject headings: planets and satellites: detection

1. INTRODUCTION

Our own solar system hosts 8 planets and 16 large (> 1000km) orbiting moons. Although more than 1,500 exoplanets have been confirmed to date, no exomoon has been detected. The question of the existence of exomoons is interesting, as it will sharpen our understanding of how "normal" our own solar system is in the interstellar context. The frequency of exomoons can also guide planetary formation theory. Lastly, some exomoons might even be habitable (Forgan & Yotov 2014; Hinkel & Kane 2013).

Various search methods have been proposed (see e.g. Heller (2014), and references therein). In what follows, we focus on two photometric methods, dubbed the "orbital sampling effect" (OSE) (Heller 2014), and the "scatter peak" (SP) (Simon et al. 2012). We will show that both complement each other and that *Kepler*-quality photometry is sufficient to detect individual candidate exomoons with the OSE.

2. METHOD

Planet transits are generally stacked to increase the signal-to-noise ratio. The OSE and SP also make use of stacking: After adding up many randomly sampled observations, a photometric flux loss appears in the phase-folded transit light curve, reflecting the moon's blocking of light. The effect depends mostly on the moon's radius and planetary distance. The OSE can be used to detect a significant flux loss *before and after* the actual transit (if present), which might be indicative of an exomoon in transit. The basic idea is that at any given transit the moon(s) must be somewhere: They might transit before the planet, after the planet, or not at all – depending on the orbit configuration (Sato & Asada 2009). But by stacking many such transits, one gets, on average, a flux loss before and a flux loss after the exoplanet transit (Fig. 1). The effect during planetary transit is undetectable in the limb-darkened noise, as there is no nominal baseline to compare it to. The shape-over-time on ingress and egress, and the depth of this flux loss then reflect the total radii and orbits of the exomoon(s), assuming high enough data quality (Fig. 2).

On the negative side, the OSE can only detect a subsample of all moon configurations: It requires the moon to be in a near sky-coplanar orbit to allow for the moon transiting the star (Sato & Asada 2010). Among the large solar system moons, 4 out of 16 have inclinations over 1°: Earth's moon (5.5°), Triton (130°), Iapetus (17°) and Charon (120°). If this rate is typical, then the OSE would work for the other ∼75% of cases.

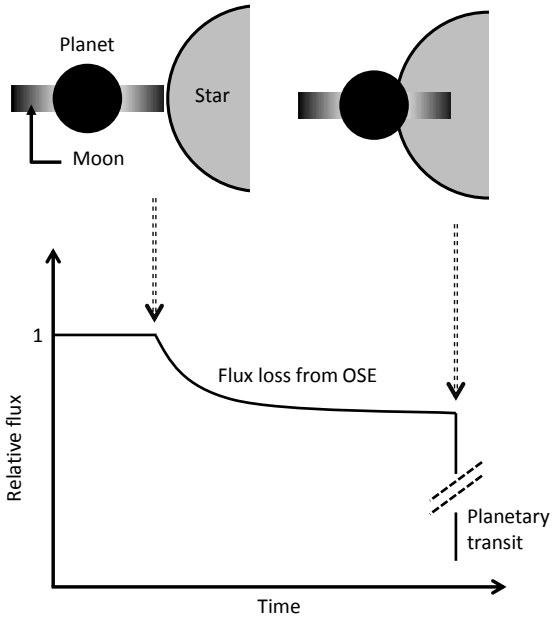

Fig. 1.— Simplified sketch of the OSE in a phase-folded plot. Top shows the star-planet-moon configuration in the line of sight, where the sampling generates a flux loss before planetary ingress (bottom).

While the presence of a significant flux loss might be an indication of a transiting body, it could also be caused by other sources, such as imperfect detrending of data or simple numerical fluctuations. It is therefore beneficial to have an (almost) independent method at hand for vetting purposes. The SP method is based on the fact that the geometrical exomoon configuration is very likely different during every exoplanet transit: On some transits, the moon might be ahead of the planet, on other transits behind it. When stacking many transits, at a given phase folded time, one gets a flux loss in some cases, and not in others. This results in increased scatter (photometric noise) when compared to out-of-transit times (Fig. 3).

hippke@ifda.eu

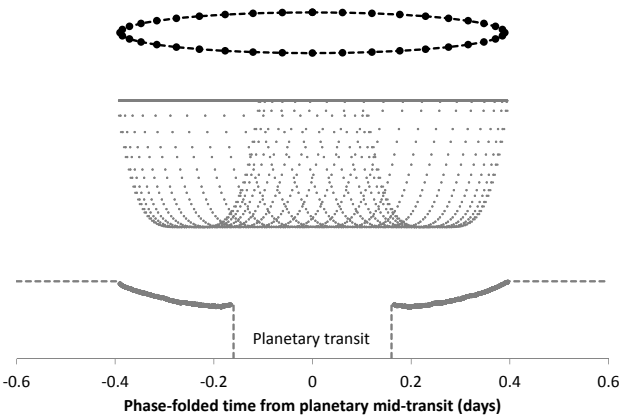

FIG. 2.— Numerical simulation of the OSE in a phase-folded plot. The circular moon orbit (top) causes higher sampling at times away from planetary mid-transit. Each dot on the orbit triggered one transit in our simulation, at the given time, overplotted in the middle. When averaging the flux over time, the OSE emerges (bottom). Just before planetary transit, the moon shows prominent egress, resulting in a "horn", which can be an indication of real exomoon presence in data, if detected. In this example, the moon orbit is circular and has zero eccentricity and inclination, resulting in a mirror-symmetrical configuration. The jitter in the OSE curve is due to the sampling of "only" 40 transits.

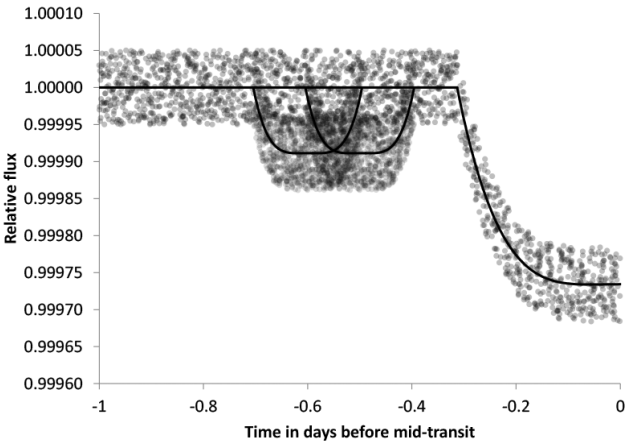

FIG. 3.— Simplified sketch of the SP effect in a phase-folded plot showing a stack of 3 epochs. During one epoch, no exomoon transit occurred (straight line at flux=1). During the other two epochs, exomoon transits occurred before planetary ingress, centered at -0.6d and -0.5d. Data points with noise (dots) show higher scatter during this phase-folded time. After stacking many transits, the scatter peak would be sampled as described by the photometric OSE. For clarity, the noise shown here is much lower (by a factor of 10) than ideal *Kepler* noise.

It is important to note that the OSE is only sensitive to *flux loss* (and not the scatter), and the SP includes a median-filter to subtract the actual flux loss (if any), and is thus only sensitive to the *scatter*. This makes both methods independent and complementary. Future theoretical advantages might allow simulations which take both effects into account by using Monte-Carlo runs to simulate various planet-moon configurations and the resulting OSE+SP, and providing a best-fit model for the given data, taking into account both flux loss and the corresponding increase in variance (René Heller (2014), priv. comm.).

2.1. *Maximizing exomoon detection efficiency*

A literature search has brought up only one example for an application of the OSE to real data (Heller et al. 2014); a null result for KOI189.01. For the SP, no application could be found. Thus, no significant experience on potential error sources is available. In the following, we have tried to account for all relevant potholes, but (as is always the case), there might be further tests required. We consider the methods and tests in this work as not matured enough to claim any exomoon detection. We will present our test results using several candidates as examples. The advantage of our approach is that only minimal CPU time and human labor (< 1hr per candidate) is required, after the required tests are established and implemented in software. Then, our framework can select candidates from a large sample, and suggest these for an in-depth analysis using photodynamic modeling as established by Kipping (2011). This modeling requires ∼50yrs of modern CPU time for a single moon, plus considerable human effort to assess the Bayesian evidence of the result. By pre-selecting promising candidates for the modeling, the total output (per human labor time and per CPU-year) of exomoon detections can be maximized.

2.2. *Data preparation*

We employed the largest database available: High precision time-series photometry from the *Kepler* spacecraft, covering 4 years of observations (Caldwell at al. 2010). Based on a list of all confirmed (821) and unconfirmed (3,359) transiting *Kepler* planets (Wright et al. 2011)[1], we downloaded their *Kepler* long-cadence (LC, 30min) datasets. For the OSE, LC data is equally well suited to SC (short cadence, 1min) data, because the effect is spread over a long (≫30min) time. The stacking of many transits and subsequent binning makes it irrelevant where exactly the "missing photons" are placed. For the SP however, SC data is preferable, due to the smearing effect (Simon et al. 2012). The background is that, on average, half of the flux loss during ingress and egress is shared with nominal flux, if the bin size is too large. The subsequent scatter measure is then less sensitive.

As LC data only requires 1/30 of the SC space and processing time, we have only processed SC data for those candidates that triggered an OSE. The bluring effect also causes additional errors on a planet (and to a lesser extent moon) fit; but the errors are small and most relevant for short transit durations. Usually they cause an error of ∼0.01% for the planetary radius, much smaller than the formal errors from an adjusted fit (Gilliland et al. 2010).

2.3. *Automatic Data processing*

The detrending for our fully automatic routines was very conservative by only fitting a line to each *Kepler* quarter and star (while masking times of transits), and normalizing the pre-search data conditioning (PDCSAP) (Smith et al. 2012) flux. Only for interesting candidates we have manually detrended the raw SAP flux data, to check for potential PDC conversion errors. The

[1] www.http://exoplanets.org, list retrieved on 18-Nov 2014

result was visually inspected, and all those stars deviating from a flat baseline were directly rejected from further analysis. This decreased the number of candidates, but avoided complicated (and often ambiguous) detrending of e.g. (often partially) variable stars, or complicated instrumental trends.

For the remaining 2,328 exoplanets, phase-folds and scatter measures were calculated in 10 bins before and after the transits. The bin width was 0.5 transit lengths, with the exception of the two bins directly before/after the planet transit, which were shortened to avoid contamination from transit timing or transit duration variations.

We will present the results from processing all planets in section 3. Afterwards, we will discuss the framework of tests for false positives (section 4) and apply this toolbox to example candidates in section 5.

3. RESULTS FOR PROCESSING ALL PLANETS

We created a combined phase-fold of all useful data, to search for an average exomoon effect. For the 2,328 transiting exoplanets with good data quality, the transit duration was transformed to unity, and the flux was measured in 10 bins before and 10 bins after the phase-folded transits. The bin width was 0.5 transit lengths, with the exception of the two bins directly before/after the planet transit, which were shortened to avoid contamination from the actual transit. Then, we added a buffer of 10% of the transit duration both before and after the transits to be excluded from any further analysis, so that any transit duration uncertainty, or transit timing/duration variations are also excluded from mismatch with exomoon flux loss. By visually inspecting all phase-folds, we removed several candidates that showed excessive TTVs/TDVs. We tried normalizing the transit depths, but found this only added noise.

To sum up, all transits of all planets were transformed in width to one big meta phase-fold ("super-stack"). We have then examined the flux of this before and after the actual transit, in order to search for flux loss caused by exomoons, as described by the orbital sampling effect.

3.1. *Data cleansing*

The resulting data were strongly dominated by outliers. This is understandable as many factors contribute to different transit depths, and noise levels: The size and apparent brightness of the host star, the size of the planet, stellar variability on a scale lower than rejected by our visual inspection, instrumental differences, and others. We decided on a set of filters to remove outliers, and included the stellar brightness ($<$ 13mag in J as measured by 2MASS), the scatter per star (we kept the better half), and the data completeness (we required 80% of the *Kepler* spacecraft duty cycle). Accepting all stellar brightnesses, and all data completeness levels does only slightly deteriorate the results. This is a trade-off hard to quantify, as one adds both signal (more stars) and noise (lower quality stars). We found, however, that the scatter of the individual lightcurve is of great influence. Our results are also consistent for the case of removing only the few very strongest outliers, so that we consider the data to be robust.

3.2. *Results for the "super-stack"*

We find a strong correlation of exomoon flux loss to the planetary orbital period. Fig. 4 shows our stacked flux for 652 planets with periods $< 10d$ (top) and for 177 planets with periods $35d < P < 80d$ (bottom). Short-period planets are not expected to possess moons (Cassidy et al. 2009), so that this group can be used as a reference point. However, a significant flux-loss just before and after the planetary transit is also apparent in the $< 10d$ group (and most prominent in the very shortest period planets), perhaps due to a slight leak of transit flux loss into the neighboring bins, despite our buffers. Indeed, when neglecting the bins closest to the planetary transit, the dips are gone.

When plotting only the 177 longer-period ($35d < P < 80d$) planets, an additional flux loss appears, starting and ending at $\sim$ 2 planetary transit durations. As will be explained in section 5.9, at least 15-20 transits are required before the OSE can build up in a single case. It is therefore not possible to detect exomoons with the OSE for long-period ($> 80d$) planets, neither for single examples nor for a larger sample. The results for planets with periods longer than 80d are consistent with this and show no significant dip.

For the planets with periods of $35d < P < 80d$, the effect is measured as an average flux loss of $6 \pm 2 \times 10^{-6}$ (6ppm), corresponding to an average total exomoon radius of about the size of Ganymede when transiting a sun-like star. Also, a significant scatter peak is detected, with the bins affected from the OSE having a scatter of 2.7 ± 0.2 ppm, compared to the baseline of 1.9ppm.

As stars and moons are of different sizes, this can only be taken as a very rough estimate. It is also unclear whether the non-detection for periods $< 35d$ comes from a real lack of moons, or from different sensitivities. We tend to interpret the result in the way that planets with $P < 35d$ have a lower probability for moons, and/or possess moons with smaller radii, so that the effect becomes hidden in the noise. Further studies will be required in the future, and the present result should be taken with caution. It can however be interpreted as a strong indicator for the existence of exomoons among planets with periods $35d < P < 80d$.

4. FRAMEWORK FOR INDIVIDUAL CANDIDATES

A simple dip in the data is necessary, but not necessarily sufficient for the detection of an exomoon. As will be explained in section 4.4, we have found 4 out of 56 planets to exhibit such a dip at the 95% significance level, likely not caused by TTVs/TDVs. One method would be to refer these candidates to photodynamical modeling, but this is very expensive in terms of labor and CPU-time. Therefore, we have developed a framework of tests for false-positives. This can either reduce the number of candidates, or at least rank and prioritize them for further analysis.

4.1. *Required results from the OSE*

For the presence of a moon, we propose the following criteria to be checked:

OSE1 A significant ($p = 95\%$) flux loss before and after the planetary transit.

OSE2 A significant ($p = 95\%$) trend towards more flux loss at closer to the transit than further away.

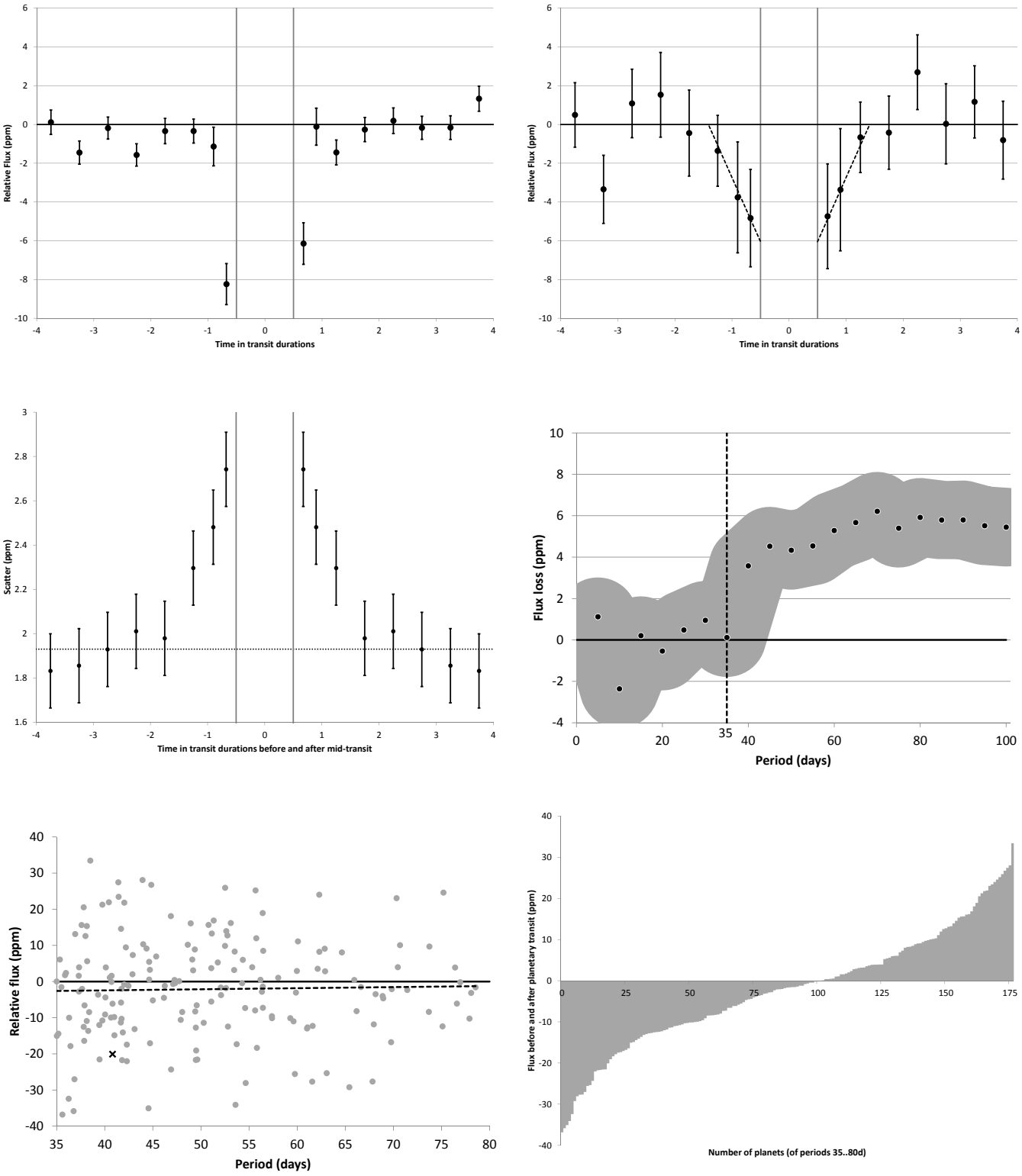

FIG. 4.— Top left: Stacked phase fold for periods $< 10d$. Flux loss is only apparent very close to the planetary transit. Top right: Periods $35d..80d$ with flux loss in neighbouring bins. Dashed line shows a symmetrical linear regression. Middle left: Scatter peak for periods $35d..80d$ is clearly detected, here shown in symmetrical form. Middle right: Cumulative flux loss (positive values) depends strongly on the planetary period. The exomoon effect from OSE is visible for P$> 35d$ (vertical line), exceeding the uncertainty (grey shading) for P$> 40d$. Bottom left: Planetary period versus flux loss/gain. While any flux gain is likely caused by noise, it shows the high overall scatter of this work. The average (linear trend as dotted line) shows significant ($p = 0.048$) flux loss. Kepler-264b is marked with a cross. Bottom right: Histogram of planets between 35 and 80d periods. Of the 176 planets, 101 show a flux loss (57%). While many of these might be false positives (also on the plus side), the distribution is already significantly skewed in a binomial test ($p = 0.029$).

OSE3 A significant ($p = 95\%$) flux loss shall not appear when only a small number of transits ($n < 10$) is treated.

OSE4 The dips before ingress and after egress shall be the largest dips in the dataset.

OSE5 The dips should not be caused by star-spots.

OSE6 The dips should not be caused by rings.

OSE7 The amount of flux loss needs to be physically plausible.

C1 The signal shall not be located in a small part of the data only, but be contained in $> 50\%$ of it.

The choice of significance level can of course be varied, depending on the data quality and the capacity for follow-up analysis. Planets on very short orbits are increasingly unlikely to host moons, due to mass loss (Cassidy et al. 2009), very small Hill radii, and orbital decay due to tides (Barnes & O'Brien 2002). As the range of stellar and planetary temperatures, masses and radii is large, a single limit cannot be given; estimates are in the range of 5–15 days for the minimum orbital period of the host planet. For long-period planets there are not enough transits in the data for the build-up of the OSE. For a minimum of 20 transits within the 4 years of *Kepler* observations, the maximum period for possible detection is then 73 days. Taking only planets with periods of 15–73 days, we have 311 confirmed planets plus 958 "Kepler Objects of Interest" (KOIs). Using the traditional 95% level significance level, and detecting a dip both before and after planetary transit, one can assume a total of $0.0025 \times 1269 = 3$ false positives, a number which can further be reduced with the other tests in our framework. Therefore, we suggest to be relaxed towards the requirements and also accept partially negative test results, especially as the tests sometimes yield *false negative* results.

Regarding OSE1, it is useful to treat ingress and egress separately, and also binned together (section 5.2). As shown in Fig. 2, the dip has a defined shape, most strongly depending on the number of moons, their radii and semi-major axis. As these parameters can only be estimated, we suggest to perform a test (OSE2, section 5.3) for the slope: The flux loss should be greater towards planetary transit, than further away from it. Furthermore, such a dip emerges only after sampling a sufficient number of transits. This can be tested (OSE3, section 5.4), together with numerical simulations for the number of transits required. Then, when the dips have been established as genuine, we need to make sure that such is not common within the dataset: The two dips should be, ideally, the largest in the whole dataset (OSE4, section 5.5).

After this step, in case the dips could not be explained away as simple numerical fluctuations or outliers, we shall consider a physical cause. Dips can be caused by star spots (OSE5, section 5.6) or, more interestingly, by rings (OSE6, section 5.7). If these can be ruled out (or appear unlikely), we shall seriously estimate the actual star-planet-moon configuration and its stability, to check whether the system is physically possible, plausible and stable (OSE6, section 5.8). Inspired by Kipping et al. (2014b), we also employ a useful data consistency check, demanding that the signal should be spread broadly in the data, and not be located in only a part of it (C1, section 5.9).

4.2. *Required results from the SP*

Equally, we define the following criteria for the detection of a scatter peak:

SP1 A significant ($p = 95\%$) scatter peak before, at and after the transit.

SP2 Shifting the period shall not significantly decrease the scatter peak.

SP3 Accounting for TTVs and TDVs.

SP4 The strength of the scatter peak shall be astrophysically plausible, and scale with the amount of data used.

C2 The signal shall not be located in a small part of the data only, but be contained in $> 50\%$ of it.

While SP1 is self-explanatory (section 5.10), SP2 and SP3 (section 5.11) are more complicated as the transit folding might not be perfect due to uncertainties, TTVs and TDVs. Lastly, as for the OSE, the amount of scatter should correspond to the estimated star-planet-moon configuration, and it should be be spread over all of the data (section 5.12).

4.3. *Manual detrending and baselining*

The initial automatic search process had only employed a linear detrending and normalization, which is sufficient to reject the vast majority of negative candidates. For the remaining interesting candidates, however, great care must be taken regarding detrending and baselining. Usually, the baseline used for transits is the time immediately before and after the transit. This method, by definition, renders the orbital sampling effect invisible. Instead, we need to derive the baselines from times long (> 2 transit durations) before and after the actual transits. The detrending must also protect not only the times of transit, but also at least two transit duration before and after the transit, in order not to smooth out any flux loss. Wrongly detrending right though the (moon and/or planet) transit dips destroys the OSE: The fitted curve goes deeper (as influenced by the dip), and thus the resulting detrended data is higher in flux, so that any flux loss from (averaged, stacked) OSE is lost.

We examined both the raw *Kepler* data (Simple Aperture Photometry, SAP) and the Presearch Data Conditioning (PDC) result of the *Kepler* data analysis pipeline. The latter tries to remove discontinuities, outliers, systematic trends and other instrumental signatures, while preserving planet transits and other astrophysical signals. It uses a Bayesian Maximum A Posteriori (MAP) approach "where a subset of highly correlated and quiet stars is used to generate a cotrending basis vector set which is in turn used to establish a range of reasonable robust fit parameters." (Smith et al. 2012).

TABLE 1
Detrending parameters for the candidates

Parameter	241b	241c	264b	367.01
Median boxcar [days]	1.0 - 2.0	1.0 - 2.0	2.0 - 3.0	0.2 - 1.0
Masking [% of transit durations]	150 - 300	150 - 300	150-200	150 - 300
Visual fit quality	Very good	Very good	Bad	Excellent
Same result from polynomial detrending	Yes	Yes	Yes	No

Parameter ranges give very similar results.

For the SAP data, we removed outliers with a sliding median and a 3σ filter. Afterwards, we tried two common detrending methods with both data sources. First, we subtracted a least-squares parabola fit to an appropriate time before and after mid-transit (e.g. Santerne et al. (2014); Gautier et al. (2012)). For Kepler-264b, we used 3 days before and after. Alternatively, we applied a sliding median to the whole dataset (e.g. Carter at al. (2012); Tal-Or et al. (2013)). For both methods, we removed data points affected by other transiting planets in the system, if present. Also, to protect the very slight putative moon flux loss, we blinded the detrending algorithm for the time span of 1.5 transit durations from mid-transit, so that it could not remove such a dip. For Kepler-264b and the median detrending, a boxcar length of 2-3 days was optimal, as it steps over the blind period and still adapts to trends on the order of a few days. For best results, these times need individual adjustments for each candidate. It is important to ensure that an adequate range of detrending parameters gives similar results, in order to qualify the chosen detrending methods and parameters as robust. A useful cross-check is to slowly shrink the protected flux area, and/or shorten the boxcar length of a sliding median detrending. As a consequence, the OSE must vanish, as the detrending adapts more and more to putative slight moon dips, and removes them.

We find that the results are consistent with SAP and PDC-SAP data, but not always for parabola (polynomial) and median detrending, as listed in Tab. 1. The PDC-SAP data gives less noise, as is expected due to the additional co-trending vectors which effectively remove instrumental trends. Most of the noise in PDC-SAP is likely due to astroseismic jitter – section 5.6 will discuss the (likely) rotational period of e.g. 11.1d for Kepler-264, accounting for an amplitude of 81ppm with strong sidelobes.

For reference, we show the detrending results for PDC-SAP data and both detrending methods for Kepler-264b in Fig. 5. The results differ only slightly. Unfortunately, these detrending methods cannot be used for the scatter peak, as will be discussed in section 5.10. We list the range of adequate detrending parameters in Tab. 1. We also release an interactive spreadsheet[2] for the interested reader. In this sheet, masking times and boxcar length can be modified, and the resulting flux loss is displayed instantly.

4.4. *Sensitivity*

We have performed a deep analysis for a sample of 56 planets, in order to derive limits for the sensitivity to an exomoon with respect to the stellar radius, stellar brightness and host planet size. We included interesting suitable examples from previous searches (Kipping et al. 2013a,b, 2014a,b; Heller et al. 2014) with periods between 15d–80d. These were Kepler-231c (KOI-784.01), KOI-314.01, KOI 314.02, KOI-463.01 and KOI-189.01; all with null results as expected. In addition, we selected mostly planets around M-dwarfs, as they exhibit deeper transit depths due to their smaller radii, plus some randomly chosen planets in order to explore the parameter space of sensitivity. This doubles the sample of currently examined planets (Kipping et al. 2015). For the limits, we assumed a circular moon with zero inclination and eccentricity, on a medium-wide orbit of two planetary transit durations, which corresponds, on average, to a semi-major moon axis as 30% of the Hill radius. We have used a custom median detrending for each candidate. Fig. 6 shows the results, presenting 2σ (95% CI) upper limits. In the best case, the OSE method is sensitive down to $R_{☾} \sim 0.32 R_{\oplus}$, which is almost the size of Earth's moon. In 6 of 56 cases, the method is sensitive to a Ganymede-sized moon, in agreement with Kipping et al. (2009). The sensitivity correlates strongly with the stellar brightness and radius, as well as the planetary radius. We suspect that the latter correlation is due to a selection effect, as the smallest *Kepler* planets are detected around suitably quiet stars with high S/N.

To illustrate the data quality and approach, Fig. 7 shows the null result for KOI-189.01, confirming the results from Heller et al. (2014), but now giving a sensitivity limit. The 2σ upper limit in this case is a high $R_{☾} < 0.84 R_{\oplus}$, suffering from the relatively dim host star (K_P=14.4). Furthermore, we have created numerical simulations for a range of moon semi-major axes, in order to explore the parameter space with regards to detectability. As can be seen in Fig. 9, larger orbits are more easily detected. Of course, the total flux loss (in photons of all photometry) is always the same, so that the integral, i.e. the area under each curve is identical. The major difference is the shape of these curves: Longer orbit moons have their ingress and egress (with less averaged flux loss) during planetary transit. During this time, the signal cannot be used, as there is no baseline. Thus, it is beneficial that the signal loss occurs outside of planetary transits, making larger separation moons easier to detect (despite their flatter transit curves). Also, their more prominent exposition of the "horn" (which is the flux gain caused by their ingress/egress towards planetary mid-transit) can aid to distinguish between (shapeless) numerical fluctuations and a real OSE.

We found six candidates with a significant flux loss, and discuss these in-depth in section 5. Out of these, two or three are identified as likely false positives. For reference, we have also found 3 planets to exhibit a significant (95% CI) flux *gain*, consistent with statistical expectations.

Depending on the orbit configuration, approximately 50% of the signal coming from moon transits is lost,

[2] Insert URL here

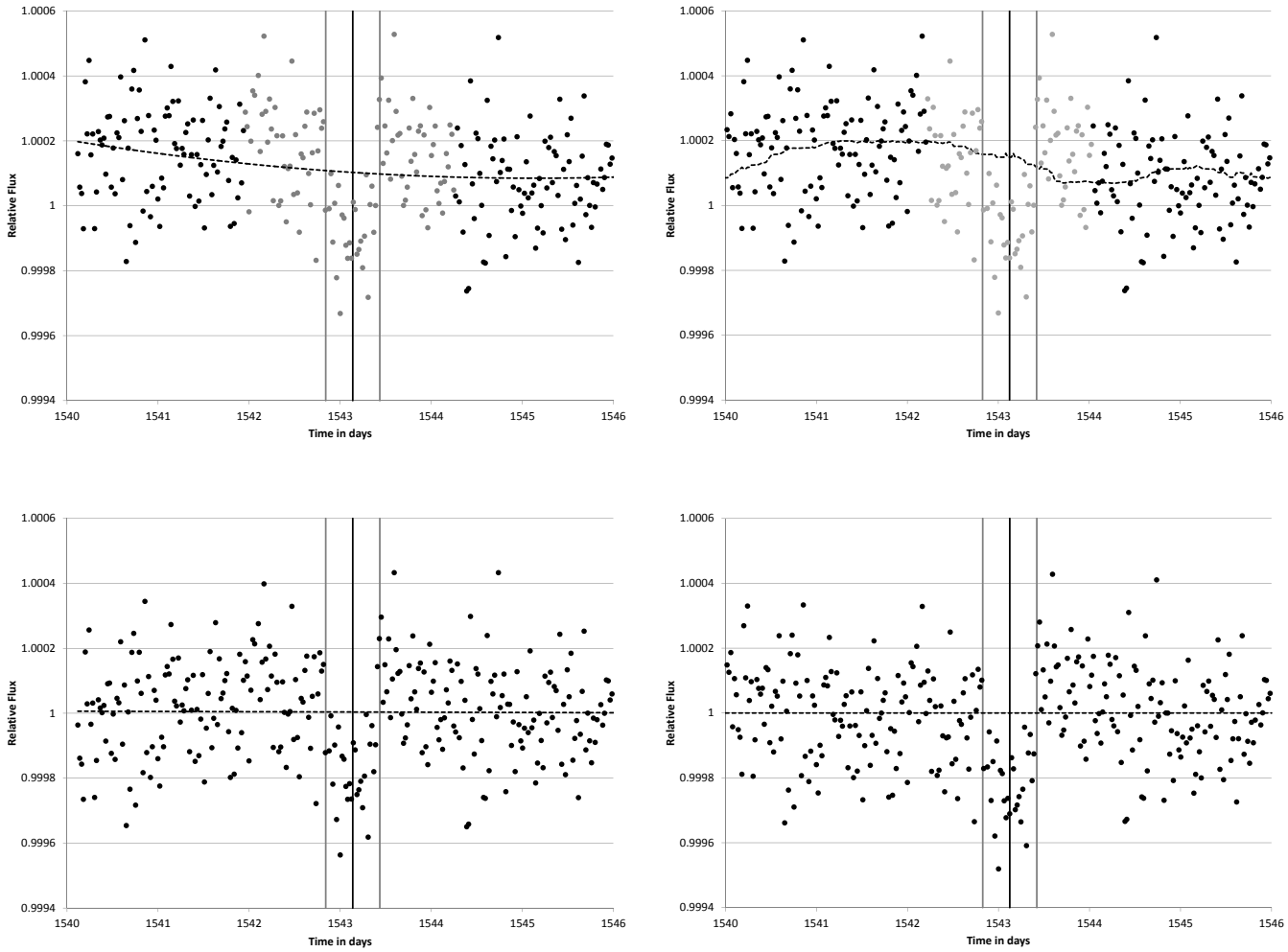

FIG. 5.— Detrending with a parabola (left) and sliding median (right) of the last recorded transit of Kepler-264b at Barycentric Julian Date ∼ 1542 (MJD-2454833). Grey dots are excluded from the fit to protect the potential flux loss from the OSE (top). Bottom: The parabola result has an average normalized flux (excluding transit and potential exomoon time) at slightly above 1, which has to be harmonized for every single transit individually, so that the flux for the time long before and after the transit is set to 1. Note that the results from both methods are very similar, which is a useful consistency check.

due to the simple fact that the sampling includes non-transiting events (Fig. 9). On the other hand, the *effective* loss (compared to photo-dynamical modeling) is less than 50%, because the OSE can leverage stacking, which reduces time-correlated noise. Of course, this applies only to moons where the OSE is sensitive to, as discussed in section 2.

4.5. *Shape of the OSE*

The shape of the phase-folded orbital sampling effect varies mainly with the moon's radius, its semi-major axis and the orbital configuration of the system. For a single-moon case, Fig. 8 shows the three main cases and their OSE curves: A near co-planar configuration is the simple case, and can server as the standard hypothesis. This is what we found among 75% of large solar system moons, as discussed in the introduction. It has a symmetrical shape varying in depth and width depending on the semi-major axis (compare also Fig. 9).

The second case is an inclined moon, tilted towards the observer. This configuration results in a still symmetric OSE, but greatly reduced depth and thus detectability. The greatest difference in shape is during planetary transit, making this configuration hard to distinguish from the co-planar case (this is because the OSE cannot be observed during planetary transit).

A more severe case is eccentricity (or an inclination shifted laterally from the observer), as shown in the bottom panel. The resulting OSE is highly asymmetric, showing that cases with flux loss on mainly one side are not necessarily false positives. In practice, with noise added, one would find *no dip* on one side (ingress or egress), and a *regular* dip on the other side with the best possible *Kepler*-quality data.

With *Kepler*-class photometry, we do not expect to be able to make significant distinctions between these cases. This might be possible with future instruments such as *PLATO*. However, in case of a moon found with other methods, for instance using photodynamical modelling, the postulated configuration can be cross-checked with its expected OSE curve. Both should agree, within the errors, to make it a consistent exomoon detection.

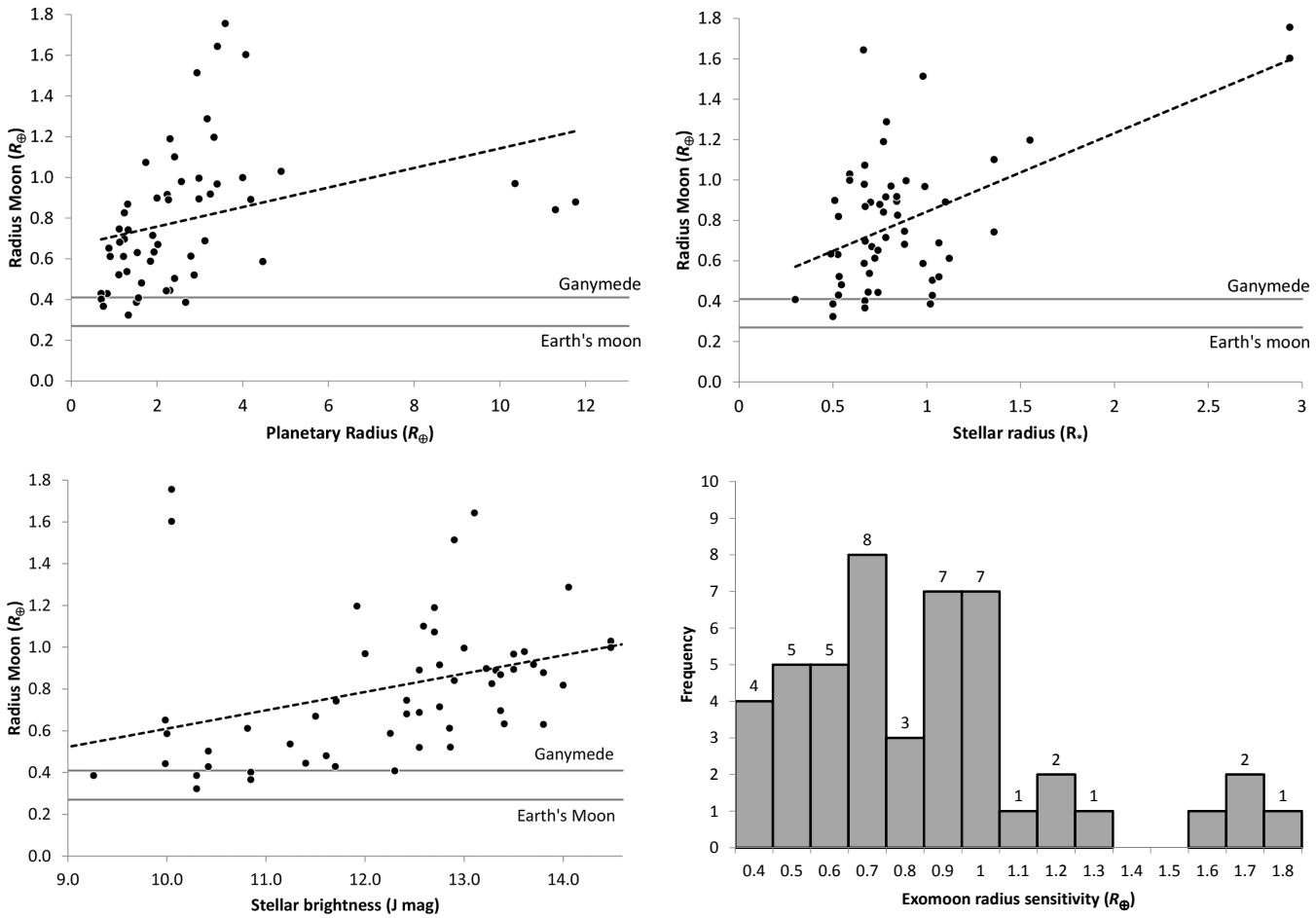

FIG. 6.— Upper limits (2σ, 95% CI) of moon radii for a sample of 56 planets analyzed in-depth, and histogram of the distribution.

TABLE 2
BEST-FIT MOON RESULTS

System	K_P	$R_*[R_\odot]$	P_P [days]	R_P [$R\oplus$]	$R_{\leftmoon}$ [$R\oplus$]	$a_{\leftmoon\,P}$ [10^4km]	Reference
Kepler-241b	15.4	0.668 ± 0.289	12.718092 ± 0.000035	2.30 ± 1.03	1.1 ± 0.1	450 ± 90	Rowe et al. (2014)
Kepler-241c	15.4	0.668 ± 0.289	36.065978 ± 0.000133	2.57 ± 1.11	1.4 ± 0.1	320 ± 60	Rowe et al. (2014)
Kepler-264b	13.0	1.550 ± 0.310	40.806230 ± 0.000540	3.33 ± 0.74	1.6 ± 0.2	660 ± 120	Rowe et al. (2014)
KOI-367.01	11.1	0.980 ± 0.185	31.578659 ± 0.000007	4.47 ± 0.55	0.8 ± 0.1	150 ± 50	Rowe et al. (2015), DV[a]
For reference: Ganymede has $R_{\leftmoon} = 0.41 R\oplus$							

[a] *Kepler* Data Validation Pipeline, http://exoplanetarchive.ipac.caltech.edu

5. RESULTS FOR THE APPLICATION OF THE FRAMEWORK TO INDIVIDUAL CANDIDATES

Our in-depth analysis of 56 stars (as explained in section 4.4) gave six candidates worth further examination. The following sections will give a brief overview to these systems, and then proceed to the individual tests.

5.1. *Candidate summary*

We summarize the six exemplary candidates in Tab. 2 and describe them in the following sections. The table and text does not include Kepler-102e and Kepler-202c. Both of these are similar to that of KOI-367.01, as they show a dip only when using a median detrending, but not when using polynomial (parabola) detrending. This case will therefore be discussed using KOI-367.01 as an example.

5.1.1. *Kepler-264b*

Confirmation of the planets b and c in the Kepler-264 system was done by Rowe et al. (2014) using data for Q1–Q15. We find identical results, within the errors, for Q1–Q17. Both planets b and c are best described as warm/hot Neptunes. As can be seen in Fig. 10, a single (non-stacked) transit does not provide sufficiently low noise even for a detection of a large exomoon. During the operation of the *Kepler* spacecraft, a total of 36 transits occurred. We could use a total of 27 transits, while 9 were lost to data missings.

As in Rowe et al. (2014), we only find insignificant TTVs and TDVs on the order of a few minutes, for both planets b and c, as is expected in such relatively long-period configurations (Awiphan & Kerins 2013). We have tried the further processing described in this paper with and without adjusting to these insignificant variations, and get identical results, both for the OSE and the SP method. Following results are thus derived from the

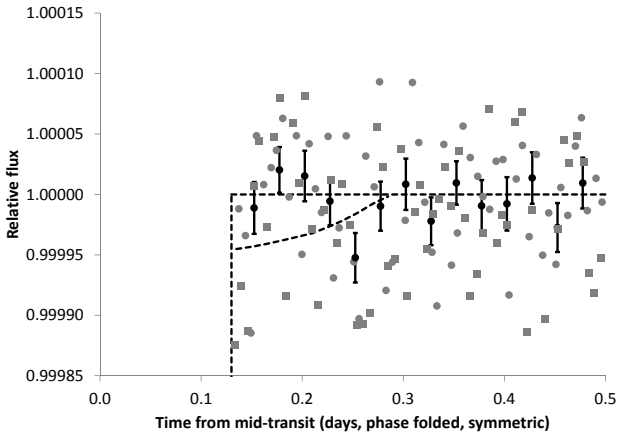

FIG. 7.— Null result (straight line) for KOI-189.01. The OSE dip shows the 2σ limit, indicating that for an exomoon detection at the 95% significance level, a flux loss of at least $R_{☾} > 0.84R_{\oplus}$ would have been required. The nominal result is an insignificant -1 ± 20ppm dip, reflecting $R_{☾} = 750 \pm 2,700\text{km} = 0.2 \pm 0.4R_{\oplus}$ (as 1σ uncertainties; obviously a negative moon radius would be unphysical).

linear ephemeris, neglecting TTVs and TDVs.

As an additional test for errors, we have added a buffer time of 2σ of the uncertainty of the transit duration before and after the transit, so that an additional time of 0.028d before and after transit was excluded from further analysis. This did not change the results significantly, so that in the following we only exclude the nominal uncertainty (0.014d) from the analysis. These TTV/TDV treatments are the same for all following candidates.

5.1.2. *Kepler-241b and c*

Two planets are known to orbit Kepler-241, a K-star with small radius ($0.668 \pm 0.289R_{\odot}$). They have periods of 12.7 (b) and 36.1 days (c), and radii of 2.3 ± 1.03 and $2.57 \pm 1.11R_{\oplus}$, making them both Super-Earths. Interestingly, we have detected a flux loss for both planets, with b being in a short orbit which might cause stability issues for moons. We have tested a wide variety of detrending parameters to check if both planets were affected by detrending issues, but found this star particularly simple to detrend: The PDCSAP flux shows only a weak (∼0.1%) flux variation, likely due to rotation and spots, on a timescale of > 10 days, which is easily and cleanly removed with a sliding median. Also, parabola detrending gives virtually identical results.

5.1.3. *KOI-367.01*

KOI-367.01 is an unconfirmed planet candidate, with the risk of being a false positive. We have included this candidate due to its significant OSE, and the high photometric quality caused by the bright ($K_P = 11.1$) host star, likely a G-star ($0.98 \pm 0.185R_{\odot}$) like our Sun. No other planets are known to orbit this star. Candidate b is Neptune-sized ($4.47 \pm 0.55R_{\oplus}$) on a 31.6 day orbit.

5.2. *Results for criteria OSE1: Significance*

The significance of the dips before ingress and after egress can be measured easily, with the only unknown factor being the duration of the dip, which depends on the orbital configuration of the moon(s). After preliminary estimation of its duration, we propose two tests:

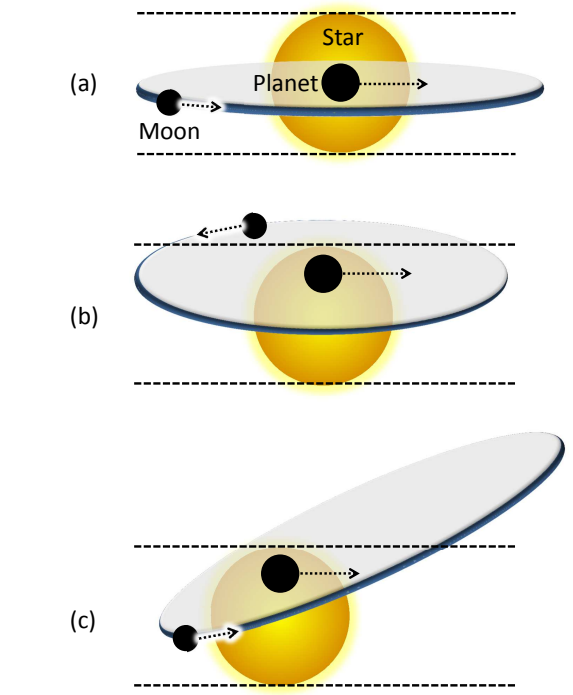

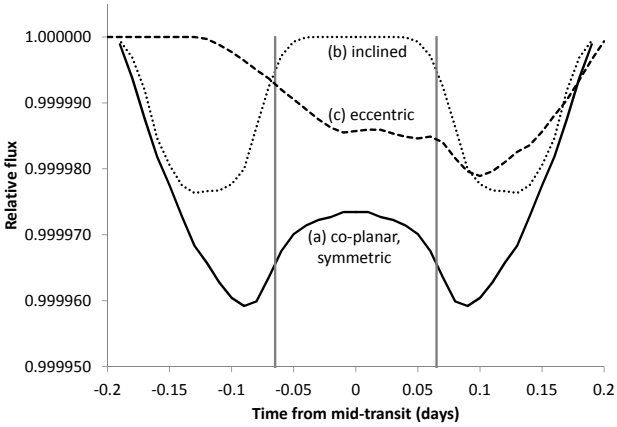

FIG. 8.— Top: Orbital configurations showing star-planet-moon: Co-planar, near-zero inclination (a); inclined (b) and eccentric (c) so that part of the moon transit is not observed (outside dashed horizontal lines). All three situations show the planetary mid-transit. In plots (a) and (c), the moon transits after the planet. In plot (b), the moon does not transit in this specific epoch. Individual transits are almost always snapshots of a given orbital configuration: The moon orbits the planet, but on a much longer timescale (days) than the transit duration (hours). Bottom: Inclined orbits (dotted) are still symmetrical, but less deep and slightly shifted outwards. Eccentric orbits (almost) lack flux loss on one side, depending on the eccentricity. Grey vertical lines show the planetary transit duration, during which the OSE cannot be measured.

One for the full length, and one for the half closer to planetary transit. This is useful because the OSE is stronger closer to planetary transit, allowing for a more secure detection. We suggest that the shorter test must be passed for ingress and egress side, and the longer test be a bonus.

For simplicity, it can also be useful to test for a bin

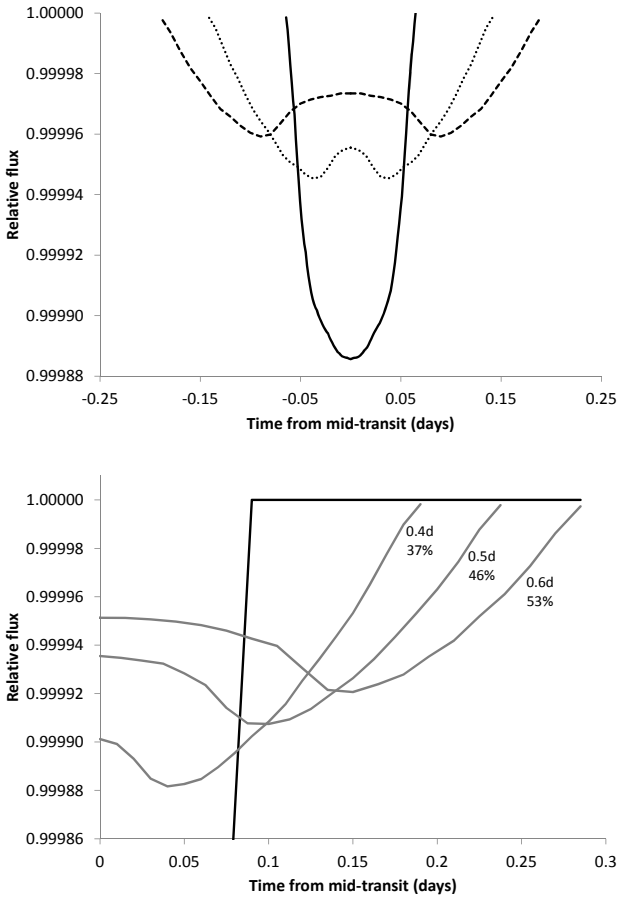

FIG. 9.— Top: Comparison of a single moon transit (solid line) and the corresponding OSE, for a wide (dashed) and a medium-wide (dotted) orbit. The integral for all three curves must be identical. Bottom: OSE dips caused by different semi-major axes of a putative exomoon $R_{☾} = 1.1 R_{\oplus}$ (grey lines) orbiting Kepler-241c (black line). Plot shows egress with moons of transit durations 0.4 – 0.6 days. The area under each moon integral is identical, but the percentages of flux loss occurring outside of planetary transit is different: Larger orbit moons are more easily detected.

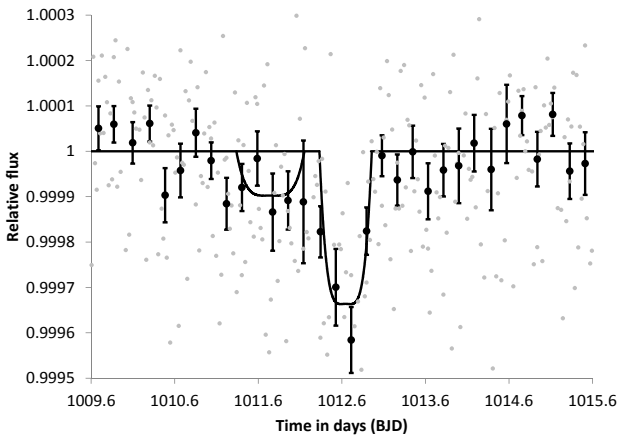

FIG. 10.— Single transit of Kepler-264b at BJD=1012.6. A potential transit curve of a hypothetical ultra-large moon (1.6 $R\oplus$) is shown before planetary ingress, with a flux of -90ppm. Such a small signal cannot be reliably detected in a single transit observation.

width of one (and: one-half) planetary transit duration, as this covers the majority of moon configurations. Indeed, for our example case of Kepler-264b, we get an estimated flux loss starting at $\sim$ |0.8|d from mid-transit (transit begins/ends at |0.297|d), so that the out-of-transit dip duration is $\sim$ |0.5|d, roughly equivalent to the planetary transit duration (0.594d).

For the data as presented in Fig. 11, results are virtually identical for both detrending methods. We get a significant flux loss during ingress (2.0σ), egress (4.8σ) and combined (4.8σ), measured as the mean of the first half transit duration before (after) planetary transit. When taking the bin width as one full transit duration, we get an insignificant flux loss during ingress (1.2σ) and still significant flux loss at egress (4.9σ). This means that the required test passed, and the optional test failed (marginally).

The results for the other candidates are summarized in Tab. 3. Every one of the others fails one or more tests, but all are significant for the data at ingress and egress binned together.

5.3. *Results for criteria OSE2: Slope*

From the sampling of the orbital sampling effect, the flux loss must increase towards planetary transit. This can be tested with a linear regression and t-tests (or F-tests) for different folded time durations, as explained in the previous section. For Kepler-264b, the slope parameters before ingress (3.1σ) and after egress (2.1σ) are both inclined towards planetary transit, and significant. The test fails for the egress side of Kepler-241b and KOI-367.01. For the ingress side of Kepler-241c, we get a marginal pass. The other sides and candidates pass the tests. The power of the individual test result should not be overestimated, as the photometry is already close to its limit.

5.4. *Results for criteria OSE3: Stacking*

During the examination of other candidate exomoons, we discovered some examples were only one or a few transits caused effects mimicking OSE and SP. One such case is Kepler-420b, where the 12^{th} transit at BJD$\sim$2455960 was affected by thermal changes on the telescope (Santerne et al. 2014). This can be tested by splitting the data in segments, and analyzing these as described above. If only part of the data seems to cause OSE and SP, it must be regarded as a spurious result.

Following the idea of Kipping et al. (2014b) to use only part of the data and check the results versus the other chunk, we have created a similar test. We ask whether a randomly chosen subsection of the data is consistent (within the errors) with the total data, so that most, and not just a few data segments contain the potential exomoon signal. This test was repeated 100 times on randomly chosen parts of the data. For our candidates, we find that any 50% of the data give the same result (a flux loss both during ingress and egress), albeit with lowered significance due to the lower number of data points. Inversely, we judge that $\sim$ 50% of the data are required for the results described here, and it is irrelevant which half is used.

In principal, OSE3 and C1 ask the same question. In this paper, test OSE3 focuses mainly on the detection of

TABLE 3
Test result summary for candidates, at 2σ (95%) significance

Test	241b	241c	264b	367.01
OSE1: Significance (l,r,b)	✓(✗) ✓	(✗) ✓✓	✓✓✓	✓✓✓
OSE2: Slope (l,r)	✓✗	(✓) ✓	✓✓	✓✗
OSE3: Stacking	✓	✓	✓	✓
OSE4: Uniqueness (a,b)	✗✗	✗✗	(✓) ✓	✗✗
OSE5: Star-spots	✗	✗	✓	✓
OSE6: Rings	✓	✓	✓	✓
OSE7: Plausibility	✓	✓	?	✓
C1: Temporal spread (OSE)	✓	✓	✓	✓

Legend: ✓Pass; ✗Fail; (✗),(✓) Marginal or partial fail/pass

outliers, while C1 will check the actual build-up of the OSE in-depth, including numerical simulations.

5.5. *Results for criteria OSE4: Uniqueness*

Ideally, there should be no other dips in the dataset that are more prominent than those before ingress and after egress. This criteria is closely connected with the actual measure of *significance* of such dips, but it is not formally the same: At any given significance level, it can occur solely from statistical fluctuations that additional dips show up, dips even deeper than the ones caused by the OSE. In a white-noise world, one could simply set a high enough significance limit to limit this – and would, in return, loose a few moon detection to *false negative* results. In a red-noise world, however, with data coming from instruments with trends, such is unwise, as it can eliminate valid information because of trends that might be *far away* temporally (and thus irrelevant, because unconnected to the signal in question). To be precise, a signal can be perfectly valid and should not be discarded because of an instrument malfunction that occurred, for example, only once and only in a distant phase-folded time.

We suggest two tests for the uniqueness of the dips in a given dataset, one hard test and one soft test. The hard test demands that one cannot shift the (virtual) folded transit time, and then still have a significant flux loss before ingress *and* after egress. To test this, one plots a phase-folded flux graph that bins the flux to a useful duration, e.g. one transit duration (of course this choice depends on the putative orbit axis). In the default configuration, one gets a dip in the first bin before and after transit. The test demands that no significant dip occurs at bin $n+1$ and bin $n-1$, with a virtual transit in a sliding bin n. As can be checked in Fig. 12, Kepler-264b passes this test.

The soft test is that the two binned dips before and after the (real) transit are the two largest dips that occur in the whole dataset. For Kepler-264b, this test is also successful, albeit only marginally. If this test fails, we recommend to plot a temporal map (like the river-plot, Fig. 19) of the relevant dips. If single outliers cause other, deeper dips, we would judge it fair to remove these (few) outliers as the likely cause.

Unfortunately, the test is less useful for short-duration transits on long periods: For a hypothetical moon around Kepler-102e, the bin width is ∼0.05d during a period of 16.1d, giving 322 bins to compare. Also, it is tedious to check and remove numerous outliers that naturally occur from numerical fluctuations (16 expected at the 95% significance level). Consequently, the other candidates fail this criteria without such clean-up. We suggest to skip the test for this category of planets.

5.6. *Results for criteria OSE5: Star-spots*

We recommend the use of the normalized PDC-SAP data to search for the stellar rotation, as it effectively removes non-astrophysical systematics in the photometry while leaving the stellar variability intact (Smith et al. 2012). Of course, the transit events need to be removed. We computed Lomb-Scargle periodograms and Fourier transforms for our candidates. For Kepler-264b, we found a consistent highest power peak at a period of 11.1±0.07 days (with the uncertainty being the full width of the peak at half maximum). This peak is accompanied by several significant sidelobes at periods between 10.5 and 12 days (Fig. 13), as is expected for an activity behavior reminiscent to that of our sun, where differential rotation causes a range of periods from 25 days at the equator to 34 days at the poles.

The OSE might be imitated by stellar spot crossings, in case the "circumstellar orbital plane of the planet-satellite system were substantially inclined against the stellar equator (...) Such a geometry would strongly hamper exomoon detections via their photometric OSE." (Heller 2014). In general, a stellar rotation period with an integer multiple of the planetary period would most strongly affect the OSE. In such a configuration, star-spots would re-occur at the same frequency as the planetary transit, creating dips in a phase-folded plot that might lie just before or after transit, resembling the OSE.

In the case of Kepler-264b, however, the closest integer multiple, $4 \times 11.1\text{d}=44.4\text{d}$, is too far off to the period of planet *b* (40.8d). We find it therefore unlikely that the OSE is mimicked by star spots. The same is true for Kepler-102e. For Kepler-241c, we find several peaks, the strongest at 12.9d and 19.1d. Smaller sidelobes are around one half, and one third of the planetary period (36.1d). In this case, it is irrelevant what the stellar rotation period in fact is: There is the possibility that star-spots cause the OSE for planets orbiting this star, and thus the test is considered to be failed for both Kepler-241b and *c*.

5.7. *Results for criteria OSE6: Rings*

Rings can form when a body enters inside a planet's Roche radius, where the body is ripped apart by tidal forces and its particles become a planetary ring. The Roche radius can be calculated as $2.4R_P(D_P/D_S)^{1/3}$, with D denoting the relative densities of planet and satellite. For plausible configurations using the values from section 5.8.5 for Kepler-264b, the Roche lobe for a planetary density of 2.9g cm^{-3} is ∼50,000km, an order of magnitude smaller than the putative moon orbit. For

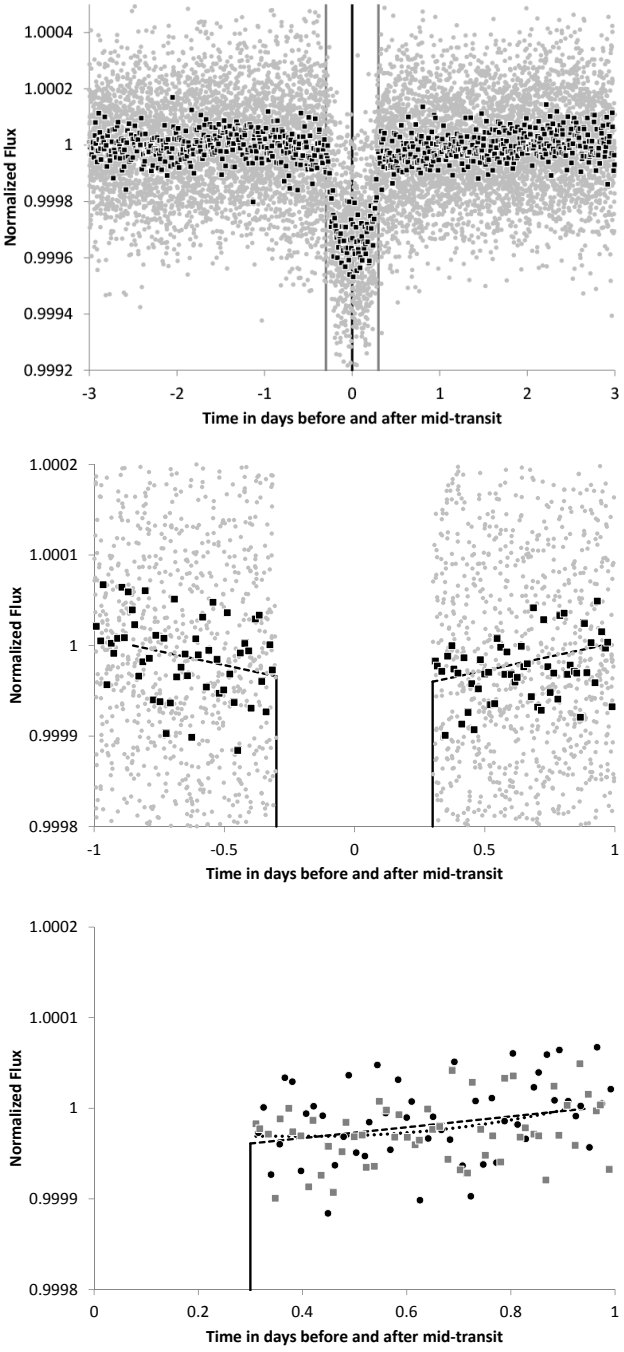

FIG. 11.— Kepler-264b phase-folded flux for a time of 3 days before and after planetary transit (top), and zoom into the region of one day before and after (middle). Grey dots are LC data, squares represent 20 LC bins. The bottom plot shows a symmetrical fold, with circles (squares) representing ingress (egress) 20 LC bins. Dashed line shows a least-squares linear fit, dottled line a numerical OSE fit (see also Fig. 14), and the vertical line the planetary transit.

lower densities, and for the other candidates which have smaller radii, the Roche lobe is even smaller. Also, rings are expected to cause both flux loss and flux gain through diffractive forward-scattering (Barnes & Fortney 2004), which is not detected for our candidates. Interestingly, the expected flux gain from rings is on the order of 80ppm for a Saturn-like planet, making detections with *Kepler*

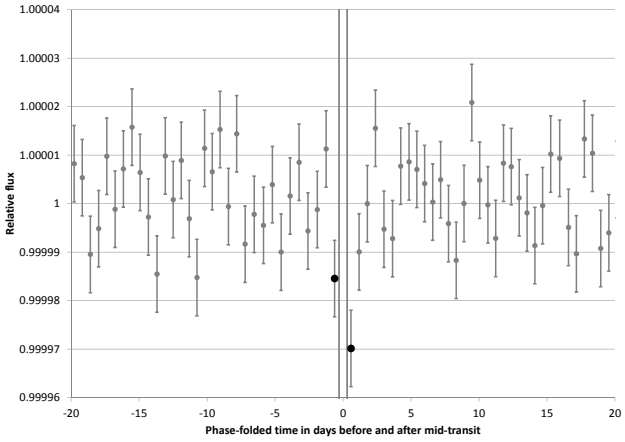

FIG. 12.— Phase-folded flux for Kepler-264b in bins of one transit duration, for the complete dataset. Planetary transit is between the grey lines. The two neighboring bins before ingress and after egress (black dots) have the highest flux loss of all bins, although the bin before ingress only marginally. Care must be taken that the bin width is adjusted so that no planetary flux loss leaks into the other bins in question. The bin during planetary transit is not shown for clarity (at ∼300ppm, it would be four times the diagram height downwards).

possible.

5.8. *Results for criteria OSE7: Plausibility and orbital parameters*

It is useful to check whether a putative star-planet-moon configuration is astrophysically possible, plausible and stable over the long time. While the possibility of any configuration is essential, the situation is less clear for the plausibility: Before the discovery of Hot Jupiters, such planets would have seemed implausible, and their discovery (Mayor & Queloz 1995) was challenged as they were found to be incompatible with theories of planetary formation (Rasio et al. 1996).

The same is true for the stability. While we should assume that most moons are stable over long (Gyr) times, there might be configurations for which this is not the case. One related example are Saturn's rings, which would be observable with *Kepler*-class photometry (section 5.7, Barnes & Fortney (2004)), and are known to be unstable on timescales of <100 Myr (Dougherty et al. 2009). Thus, instability should raise strong doubts about the presence of a moon (and less so about the presence of a ring), but does not proof their non-existence.

We suggest to derive estimates for putative planet-moon configurations, as will be explained in the following section, and then to assess the system.

5.8.1. *Fitting the data to the OSE*

A fit of the data to various exomoon parameters can be done using the analytical equations from Heller (2014) with a simple iterative χ^2 minimization. The parameter space of such a Monte-Carlo run can also include the test for multiple moons versus a single moon. With *Kepler*-data, however, we judge the differences (a few ppm) as too small for a try.

Alternatively, one can create numerical simulations, either on picture/pixel level, or on photometric level, as we

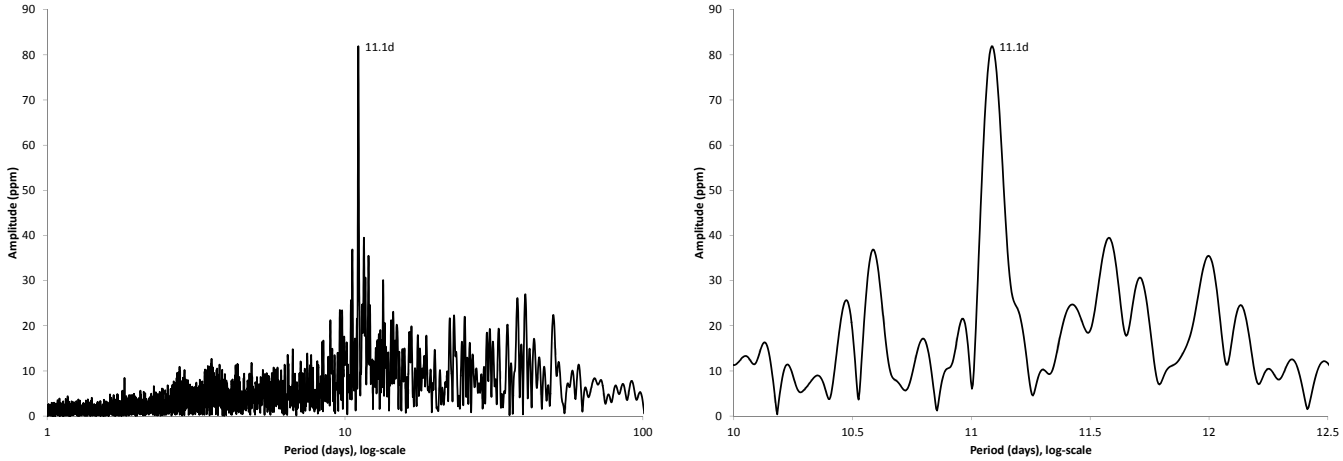

FIG. 13.— Periodogram showing the strongest peak at 11.1d (top), likely the rotational period with an amplitude of 81ppm. Zoom (bottom) shows sidelobes from differential rotation, a strong indicator for stellar rotation.

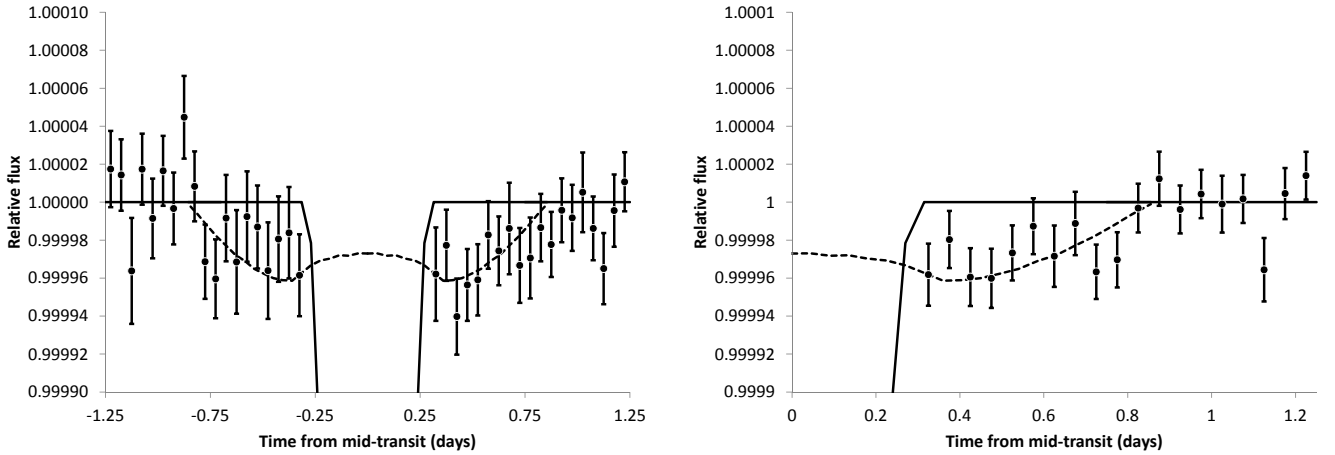

FIG. 14.— OSE fit for Kepler-264b with 1σ uncertainties. Dashed line is a numerical OSE fit. Left: Separate data for ingress and egress. Right: Binned together assuming symmetry. Best fit gives $R_{☾} = 1.6 \pm 0.2 R_{\oplus}$, semi-major axis 610,000km.

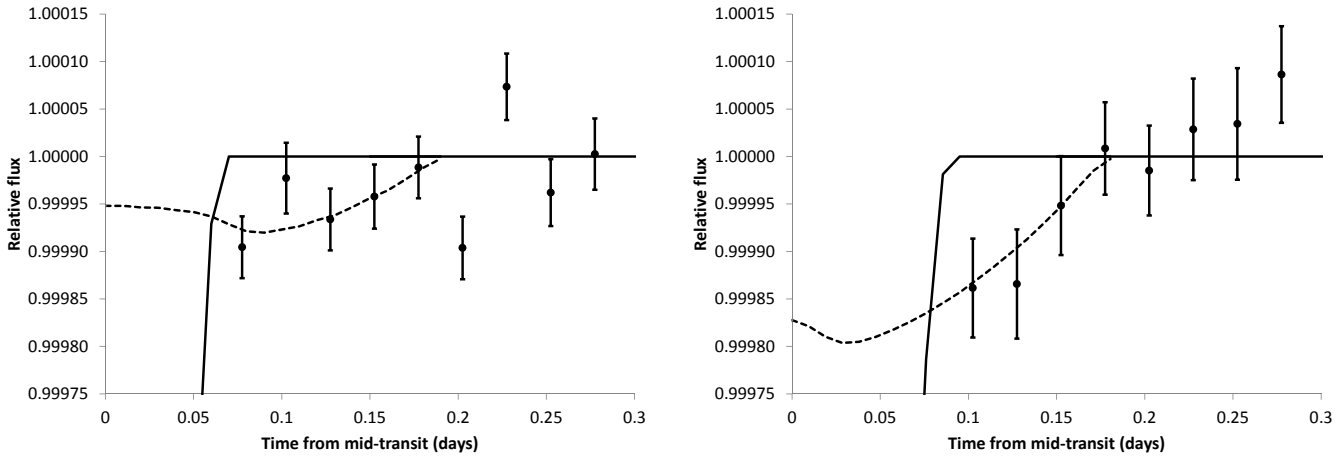

FIG. 15.— OSE fits for Kepler-241b and c, using the same scales for comparison. Left: Kepler-241b with $R_{☾} = 1.1 \pm 0.1 R_{\oplus}$, semi-major axis 450,000km. Right: Kepler-241c with $R_{☾} = 1.4 \pm 0.1 R_{\oplus}$, semi-major axis 320,000km. Planet b has $3\times$ more data due to a shorter period, and thus smaller uncertainties. Planet c has the larger putative moon on a slightly smaller orbit, causing a different dip shape with no "horn" (for a single moon solution). This is a case where a multi-moon solution would look virtually identical. From a data analyst's perspective, a moon swap between the planets would have been preferred, combining smaller uncertainties with a larger dip.

have done. This has the advantage of naturally accounting for stellar limb darkening, as one can use the as-is planetary transit shape and re-size it in width and depth for various moon sizes. This creates only minor distortions, e.g. for the transit, ingress and egress duration (as the moon is smaller than the planet), but these differences are negligible after > 100 realizations on a circular orbit for the OSE. The principle of stacking is shown in Fig. 2, and we make our software template available for the interested reader[3]. For this paper, we have only fitted single moons on circular, symmetrical cases and therefore show the following plots folded symmetrically, which increases signal-to-noise by a factor of $\sqrt{2}$.

We have performed these simulations for all four moon candidates. The best-fit results are shown for Kepler-264b (Fig. 14), Kepler-241b and *c* (Fig. 15), and for KOI-367-01 in Fig. 16. For the first and the last, we also show ingress and egress separately for illustration. Modeling has always been performed assuming symmetry, and thus binning both sides together.

In addition, we have performed a signal-injection and retrieval, as will be explained in the following section.

5.8.2. *Signal injection and retrieval*

A useful test is to use real data (including its red noise), without any transit events, and inject simulated moon transits into it. Afterwards, the OSE can be retrieved and compared to the observed result. Both should be consistent within the errors.

We have performed this for Kepler-264b, using the same number of transits (26) and randomly chosen plain time segments of Kepler-264b data. Into this data, we have injected the moon dips described in the previous section. Afterwards, we have retrieved and folded them to the same OSE. The result is virtually identical to the real data, and visually indistinguishable from Fig. 14. We have repeated this test 10 times using different segments of data, and all look very similar – some a bit above in flux compared to the real result, some a bit below. This is of course no proof that a detection is real, but it is a necessary test to check that a detection *can* be possible with the given data quality. Clearly, the real Kepler-264b data is sufficient for a 1.6 $R_\oplus$ exomoon detection.

5.8.3. *Plausibility of the OSE fits*

From the results shown in Tab. 2, it is apparent that the total moon radii are all larger than single solar-system moons. It is useful to put these results in context. We will take Kepler-264b as an example, as this candidate has the largest putative moon.

Assuming a solar radius of $R_* = 1.55 R_\odot$ for Kepler-264b and a planetary radius $R_P = 3.3 \pm 0.74 R_\oplus$, the total exomoon radii would then be ∼10,000km (1.6 $R_\oplus$) on a semi-major axis of $a_{SP}/R_P = 31 \pm 11$ planetary radii, i.e. ∼660,000km. For comparison, the Earth/Moon orbit is at 384,400km; Jupiter/Ganymede at 1,070,000km. The uncertainty of the semi-major moon axis is dominated by the planetary impact parameter $b = 0.93^{+0.01}_{-0.64}$ and the host star's radius, $R_* = 1.55 \pm 0.31 R_\odot$, which is reflected in the planetary radius uncertainty, 3.3±0.74R⊕. It is important to note that these parameters quantify the total effect, and it is unclear whether this comes from a single moon or multiple moons.

For comparison, Jupiter's largest moons Ganymede (2,632 km, 5.6ppm), Callisto (2,410 km, 4.7ppm), Io (3,660 km, 2.7ppm) and Europa (1,560km, 2ppm) would account for a flux loss of 15ppm, that is ∼50% of the required 31ppm, in case they were orbiting Kepler-264b on short orbits. Kepler-264b is almost (86%) the size of Neptune, thus making the argument for several moons more plausible. Fig. 17 shows a sketch of the potential exomoon size for the case of a single moon.

Following formation theories, such large moons would likely not have formed in situ (Canup & Ward 2006), but be captured (Williams 2013). It has also be shown that Neptune-sized planets can capture Earth-sized moons (Porter & Grundy 2011).

5.8.4. *Shape of the OSE*

The data quality is not sufficient for a detection of the "horn", where moon egress/ingress takes place just before/after planetary transit. This occurs for single moons on wide orbits. A detection of this feature might be a powerful tool used with better photometry in the future: It requires the data to not only exhibit some dip, but follow a distinct dip shape. Judging from Fig. 14, ∼2-3 × lower noise is required for a 2σ detection, indicating that such a detection is possible with *PLATO*-class photometry.

5.8.5. *Orbital stability*

Kepler-264b is the most critical case in terms of stability, as its fit gives the highest radius on the largest orbit. Therefore, we discuss orbital stability for this example.

Retrograde moons are argued to be stable up to nearly (93%) of the Hill radius (Domingos et al. 2006). Neglecting a potential eccentricity, the Hill sphere can be calculated as $r = a \sqrt[3]{M_P/3M_\odot}$, where r is the Hill radius and a the distance between star and planet. As the mass of the planet cannot be measured from the photometry, we can only derive limits for the planetary density with regards to the Hill sphere. For a Hill radius of 660,000km, the planetary mass needs to exceed 1.75g cm^{-3}, which is slightly above the density of Neptune (1.64g cm^{-3}). For a heavier composition of e.g. 2.9g cm^{-3}, as in the comparably sized Kepler-20c (Gautier et al. 2012), the Hill sphere would extend to 1,700,000km, so that the potential exomoon would lie at 39% of the Hill radius. Following Kepler's 3rd law, depending on the mass (density) of the planet, the orbital period for a 660,000km orbit would be in between 12.9 days (2.9g cm^{-3}) and 17.1 days (1.64g cm^{-3}). Planets *b* and *c* are in near 3:1 orbit resonance. The same resonance for a putative exomoon around 264b would yield an orbital period of 13.6 days and a planetary density of 2.7g cm^{-3}. Conversely, this shows that exomoons can reveal a planet's mass solely from photometry, and without the use of radial velocity measurements.

To sum up, an exomoon around Kepler-264b could be stable if the planet's density exceeds that of Neptune, which is plausible for a planetary radius of 3.3 $R_\oplus$.

5.9. *Results for criteria C1: Temporal spread*

[3] Insert URL here

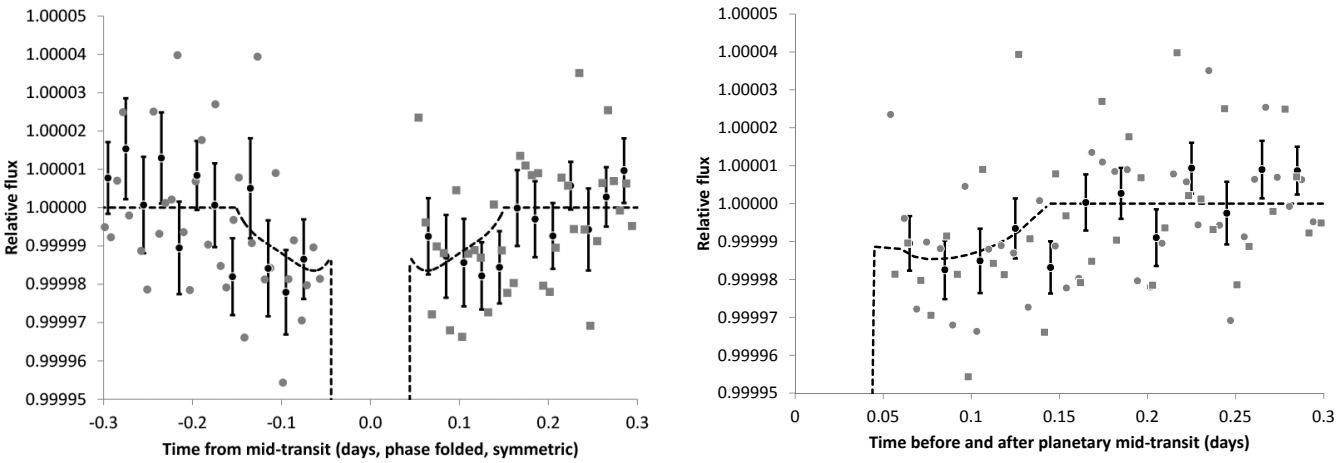

FIG. 16.— KOI367-01. Left: Ingress and egress shown separately for illustration. On the egress side, the slope test (OSE2) has failed, as the flux should decrease towards planetary transit. Right: Combined data giving a best fit for $R_{☾} = 0.8 \pm 0.1 R_{\oplus}$, semi-major axis 150,000km.

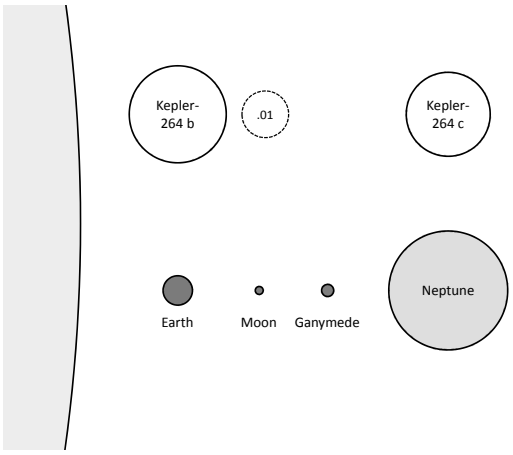

FIG. 17.— Size comparison for Kepler-264 planets a and b, together with potential exomoon .01. The bottom row shows some solar system objects for comparison. Distances are not to scale.

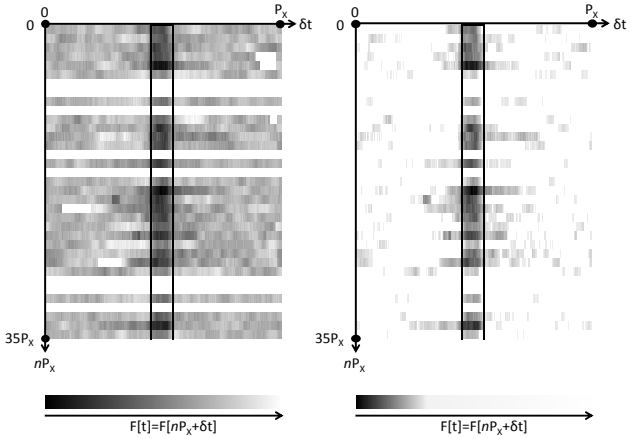

FIG. 18.— Left: River-plot for Kepler-264b. Each row is one transit (in between vertical lines); time runs from top to bottom. Darker colors are lower flux, whites in the left plot are missings. Both top plots show the same data, but with different shadings for clarity. On the right plot, it can be readily seen that the flux loss clusters before ingress and after egress. It is also evident that this flux loss is not located in only part of the data (e.g. in only one line, in only the first half), but is present all over the dataset.

In the case of *one* moon, it should only block light on some transits (not all), and only on one side (ingress or egress) per transit. Unfortunately, the photometry is at the very limit for exomoon dips on the ppm level in a single transit. We suggest to plot a "river plot" (Carter at al. 2012; Nesvorný et al. 2013), and show this for Kepler-264b in Fig. 18. In the stretched version (right panel), one tends to believe that the dips are indeed one-sided. For instance, the first row (period) shows a flux loss before ingress, while the second has only a flux loss after egress. Also, a few transits seem to lack any moon dip, as expected for those cases when the moon is in front or behind the planet, or not transiting at all (e.g., due to a non-zero inclination). However, there are also rows that show features both before ingress and after egress (e.g. row 5). What is more, some rows show features longer than possible for a moon transit (e.g. row 13).

Such noise features are also present in a null test (Fig. 19) for the phase folded time -11 days before planetary transit, where the third largest dip (after ingress and egress) in the dataset occurs, caused by numerical fluctuations. Without photodynamical modeling, which is beyond the scope of this paper, we find it hard to decide which of these features have an individual astrophysical cause, and which are instrumental trends or simple noise. Thus, we judge the river plot (the individual transit events) as neither in favor nor in disfavor of the moon hypothesis.

Another test should be made to answer the question about how precisely the OSE builds up over time. Due to the very nature of the additive sampling of the effect, which includes non-transits, the dip *cannot* be present after just a few transits. Such would indicate a numerical fluctuation. On the other hand, the cumulative flux loss should build up within the first few 10s of transits. The exact number depends on the noise floor and frequency of moon transit, but should in general be between 10 and 50. After the buildup, no further (additional) flux loss should appear, but the cumulative depth of the dip should stabilize at its final level. Additional data should

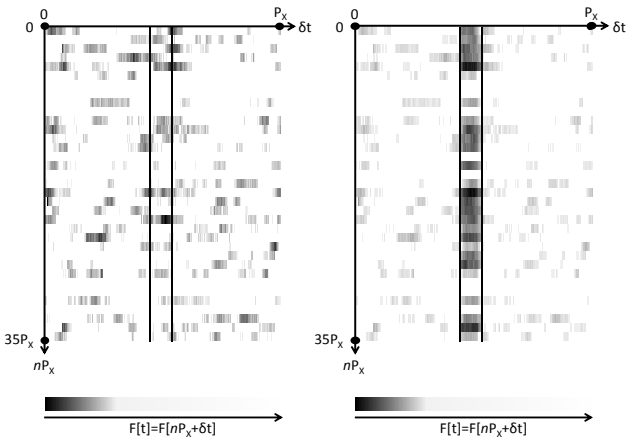

FIG. 19.— Left: River plot null test for the phase folded time -11 days before planetary transit, where the third largest dip (after ingress and egress) in the dataset occurs, caused by numerical fluctuations. Flux loss seems to concentrate on the first rows. Right: Same time and data, after injection of the transit dip. Flux loss is not apparent anymore, indicating a noise-only dip, as is expected at this time of no transit.

then only decrease the uncertainties, but not deepen the dip.

To test this, we find it useful to plot the number of transits versus the average flux loss, measured in an adequate bin before plus after planetary transit. For our example of Kepler-264b, we can see that the cumulative flux loss follows a random walk until transit #13 (Fig. 20). Afterwards, a dip begins in the cumulative data, becoming significantly negative from transit #17 on (the chart shows the 2σ (95%) uncertainties). After transit #19, the cumulative flux loss stabilizes at ∼30ppm.

For Kepler-241c, we find that the OSE stabilizes after transit #23 (Fig. 21). The progression during the first few transits is skewed southwards due to a few outliers, but then stabilizes at the final level.

Of course, the start and the end of the observations could have happened at other points in time. To test the general build-up of the OSE, we have performed a Monte-Carlo test for Kepler-264b with $N = 26 \times 10^6$ realizations to answer the question of how significant an OSE would be, on average, after only having observed randomly chosen n of N=26 transits. Fig. 20 shows the results for the 95% significance level. It can be seen that, on average, 21 transits are required for a marginal detection. A more refined test for this question would be a cumulative Bayes factor map (Gandolfi et al. 2015). From a purely statistical view, one could also ask for stationarity in the data, i.e. test whether the time series follows a random-walk (null result) or converges with a trend. To test this, we employed the Augmented Dickey-Fuller test (Said & Dickey 1984). The test rejects the random walk hypothesis for Kepler-241c at the 99.9%-level, and attributes an 80% probability for a trend in Kepler-264b. Our null test for a random walk was the same dip of Kepler-264b at the phase-folded of -11d, for which the test gives only a 10% probability to the existence of a real trend, as is expected. Such unit root tests are known to benefit from longer time-series, and the results for n=26 and n=40 should only be regarded as indicators.

To sum up, we interpret these results in favor of the OSE interpretation (over statistical fluctuations) for our candidates.

5.10. *The scatter peak*

The SP method employs a sliding boxcar median of the folded lightcurve to subtract the average transit shape. This removes any flux loss from OSE and planetary transit, and makes the SP an independent method.

Unfortunately, we find that the trends in the *Kepler* data make the analysis of the SP highly problematic. The raw SAP flux data contains instrumental trends on the order of ∼1%, rendering any scatter on ppm scale invisible. Clearly, detrending is required. The approach described in section 4.3, where the actual transit (plus a bit of data before and after the actual transit to account for TTVs and TDVs, and to protect the moon dip) is masked, creates an artificial scatter peak in itself. This comes from the simple fact that some area is not detrended as well, as it is excluded from the fit, and has thus higher noise. To check this, one can fold to a plain area of no transit (where no scatter peak can be), and detrending with excluding some data then promptly creates a scatter peak (Fig. 22).

For quiet stars, the Bayesian Maximum A Posteriori (MAP) approach (as explained in section 4.3) might be useful, as it performs the detrending using other reference stars. For our example of Kepler-264b, we are however left with noise from stellar spots on the order of ∼80ppm (section 5.6), which overshadows a 30ppm moon signal.

We have considered two methods that can be applied in such cases.

5.10.1. *Subtraction of scatter template*

As the detrending creates a scatter peak anywhere in case of blinding the fit, this false positive peak can be created n times at plain phase fold times, and its average height subtracted, like a template, from the time in question. In practice, unfortunately, the template shows a scatter increase of ∼5-50%, while the real scatter peak within *Kepler* noise is expected on the order of ∼1%. We find that after subtraction of the template, all results are spurious, and the method to be useless.

5.10.2. *Temporal cleanup*

If detrending is so problematic, one can try to avoid it and clean up the mess afterwards. This method uses the PDC-SAP data, without the instrumental trends but which still contains occasional jumps from stellar activity. The idea is to create the scatter peak plot, and an additional map answering the question of its temporal origin (Fig. 23). This map can then be used to set a useful threshold, e.g. keeping the more quiet 80% of the data. Then, one can cleanup the scatter peak plot with this decision.

For Kepler-264b, this method seems to work, as the scatter is relatively smooth afterwards. However, the noise level is still too high (at ∼50ppm) for the detection of the scatter peak, which is consistent with numerical simulations done by Simon et al. (2012). Instead of 19 periods short-cadence data, about 50 to 100 are required. We conclude that no SP has been detected, for

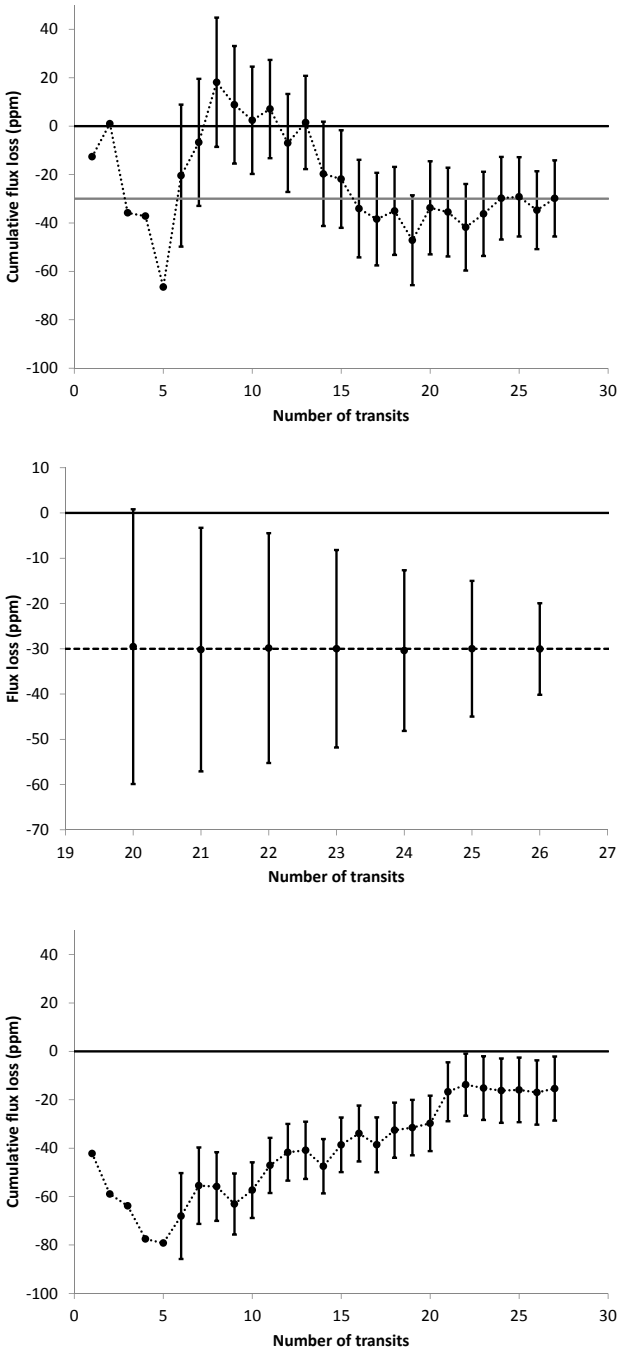

FIG. 20.— Top: Real build-up for Kepler-264b flux loss over time. After a random episode, the OSE builds up from transit #13 on and stabilizes at ∼30ppm after transit #16. Uncertainties are 2σ (95%). Middle: Monte-Carlo test asking for the average number of transits required (result: 21) for a detection at the 95% significance level. Bottom: Null test for the phase folded time -11 days before planetary transit, where the third largest dip (after ingress and egress) in the dataset occurs, caused by numerical fluctuations and/or red noise. Flux loss is only apparent at the beginning of the dataset. After only 5 transits, no OSE can have build up; proof of a false positive dip. Also, as is expected for a random-walk of noise, the trend is likely to return to zero after long enough time.

a lack of data, so that the test SP1 (significance) cannot be answered. The same is true for all other candidates. From our experience, the application of the scatter peak is not possible for stars that require heavy detrending on short (<10d) timescales. For longer timescales, very low amplitudes and very short transit durations, certain detrending methods might work, such as fitting polynomials or fully modeling the rotation with star-spots. The key is to exclude as little data as possible (during transits) from the fits. Such modeling, however, is beyond the scope of this paper.

5.11. *Results for criteria SP2: Period shift and SP3: TTVs+TDVs*

There is one major other configuration that also causes a scatter peak: Imperfect transit folding. This can occur due to TTVs and TDVs, and also when using incorrect periods. One such case is Kepler-11d, where the published period is 22.6845±0.0009d (Lissauer et al. 2013). When using this period, the median-filtered phase fold shows clear signs of a folding error in the form of "wings" during ingress and egress (Fig. 24). At first glance, this can be mistaken for a scatter peak, but the main difference is that it only appears on the time of ingress and egress, and not during the planetary transit. When correcting the period to P=22.687d, the scatter peak is completely gone. This makes for a good test: Shifting the period should not decrease the scatter peak, i.e. the scatter peak should not be removable by "correcting" the period. If it does, the period is wrong, and the scatter peak irrelevant.

Using Kepler-264b as an example, we have also tried shifting the period, and done this for ±0.1d, which is ∼190x the uncertainty of the period. Our step rate was 0.000001d. Around the best fit period, we found scatter peaks fluctuating by ±10%; an insignificant difference. Further away ($>$ |0.015|d), the scatter peak increases significantly due to sidelobes of the folding error (see Fig. 24). We conclude that the period is, within the errors, correct.

5.12. *Results for criteria SP4: Plausibility and C2: Temporal spread*

Any detection of a scatter peak must be verified with numerical simulations, in order to assure that the peak height is in agreement with the expected value. This can be done as described in section 5.8.2, by injecting transits into real data (without transits) and retrieving them for comparison.

Following criteria C1, the data can be split the data in equally sized parts and performed the SP tests described above. For a lack of scatter peak detection, we have not pursued this task.

6. DISCUSSION

As summarized in Tab. 3, no candidate passes all tests. Nominally, Kepler-264b has the best result. However, its OSE fit gives the most extreme values for the moon radius ($R_{☾} = 1.6\pm0.2R_{\oplus}$ orbiting a $3.33\pm0.74R_{\oplus}$ planet), raising serious doubt about its plausibility. While likely physically possible, it is unclear whether such a configuration can be real. On the plus side, different detrending methods give consistent results.

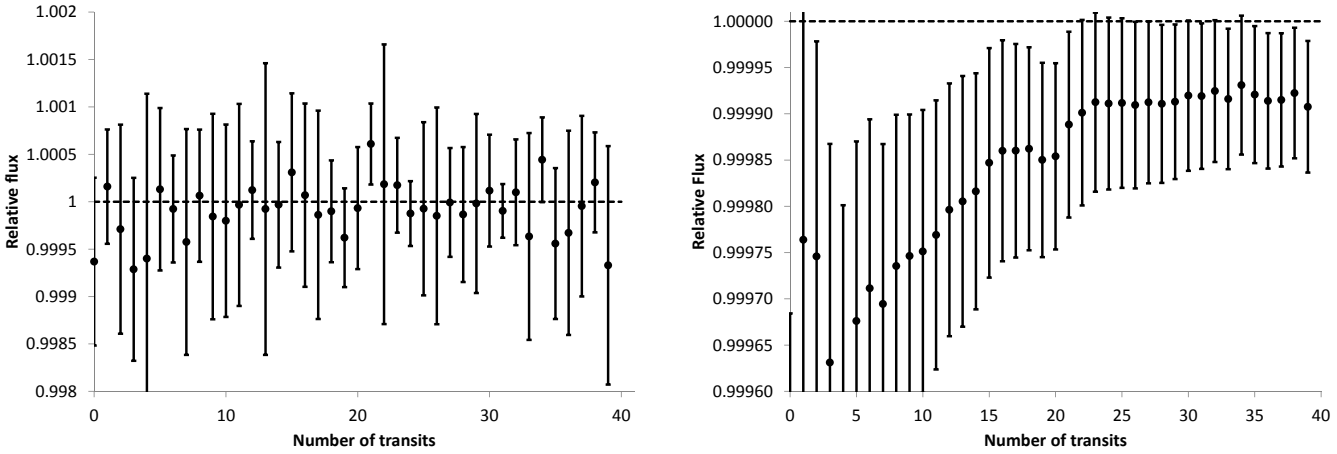

FIG. 21.— Left: Individual flux measurements for Kepler-241c for each transit (taking the average flux for a time of 0.05d before ingress and after egress of each transit). Most periods are, by itself, consistent with no flux loss. However, it is apparent that the average is below nominal flux, indicative of another transiting body. Right: Cummulative flux loss over time. After a random episode, the OSE stabilizes after transit #23.

TABLE 4
RECOMMENDED TEST ASSIGNEMENT

Test	Statistics	Plots
OSE1: Significance (l,r,b)	t-tests	Phase-folds (Fig. 11)
OSE2: Slope (l,r)	t-tests	Phase-folds (Fig. 11)
OSE3: Stacking	Monte-Carlo	River-plot (Fig. 18), build-up plot (Fig. 20, 21)
OSE4: Uniqueness (a,b)	t-tests	Phase-fold in bins (Fig. 12)
OSE5: Star-spots	Periodogram, Fourier	Time-amplitude graph (Fig. 13)
OSE6: Rings	Density, Roche-radius	–
OSE7: Plausibility	–	OSE-fit (Fig. 14, transit plot (Fig. 10)
C1: Temporal spread (OSE)	Monte-Carlo, Dickey-Fuller	River-plot (Fig. 18), build-up plot (Fig. 20)
SP1: Significance	t-test	SP-plot (Fig. 22, smoothed)
SP2: Period shift	–	SP of phase-fold (Fig. 24)
SP3: TTVs+TDVs	–	SP of phase-fold (Fig. 24)
SP4: Plausibility	Monte-Carlo (numerical)	–
C2: Temporal spread (SP)	Monte-Carlo	Scattermap (Fig. 23)

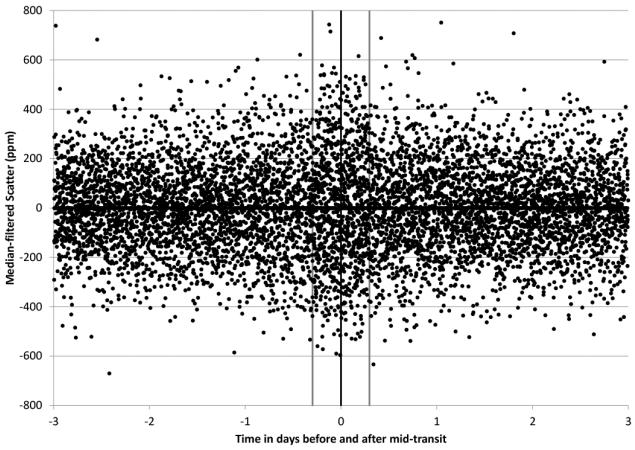

FIG. 22.— Median-filtered scatter for Kepler-264b with false-positive scatter peaks at $> 8\sigma$ significance due to improper detrending.

The "double moon system" of Kepler-241b and *c* offers more plausible, but still very large moons ($1.1 \pm 0.1 R_\oplus$ and $1.4 \pm 0.1 R_\oplus$) orbiting Super-Earths. Both candidates have limited significance of the individual dips (OSE1), and issues with the slopes of the dips (OSE2). On the other hand, both are easy to detrend and give virtually identical results for all detrending methods.

Kepler-102e shows marginal significance of the individual dips, but all slopes in the right directions. However, both are vulnerable to detrending options, with parabola detrending giving better (Kepler-102e) OSE fits. Kepler-102e raises doubts of star-spot induced flux variations.

For KOI-367.01 and Kepler-202c, the largest issue is certainly the fact that the parabola detrending gives a different result (no OSE), when compared to the median detrending. In this case, we have to assume a detrending artefact. The same is true for Kepler-102e, which also suffers from doubts of star-spot induced flux variations. On the other hand, it is interesting to note that planet *e* is the heaviest in the Kepler-102 system. One should assume that a more massive planet can host larger moons, making it the most likely moon host planet in this system of five.

The general mix of test passes and failures makes it very difficult to consider any one candidate the most promising. From statistics, we have to assume that three of the six candidates are false-positives, and tend towards rejecting Kepler-202c, Kepler-102e and KOI-367.01.

For Kepler-241b and *c*, and Kepler-264b, we recommend follow-up analysis using photodynamical modeling. For future work, we have summarized our test recommen-

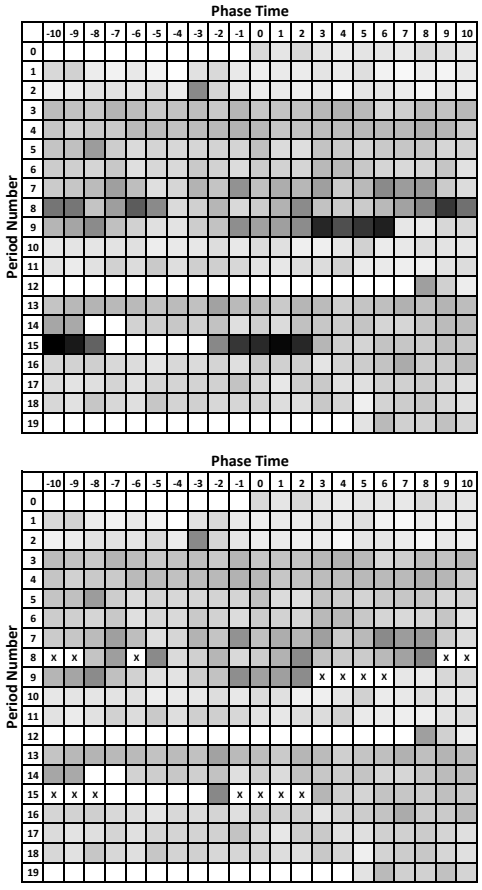

FIG. 23.— Scattermap for Kepler-264b short cadence data. On the horizontal axis, a time from -10d to +10d in the phase fold is shown, with a bin width of 1d. On the vertical axis, the 19 periods of SC data are displayed. Upper panel shows raw data, lower panel after cleanup of the 16 largest outliers (in black color before, with crosses afterwards).

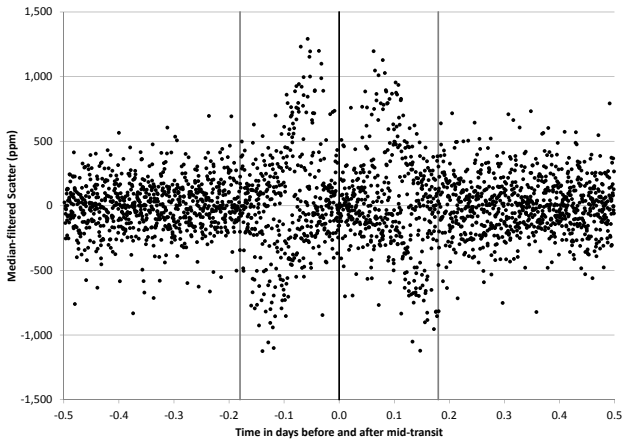

FIG. 24.— Median-filtered scatter for Kepler-11d with false-positive scatter peaks at $> 8\sigma$ significance due to an incorrect period.

dations in Tab. 4.

7. CONCLUSION

"What is not disputed, is not particularly interesting"[4] – as explained, we do not claim an exomoon detection in this paper, but only present methods and tests to consider them candidates. The detection of exomoons is at the limit of current photometry, and its methods and tests need to be checked, challenged and verified. The methods at work (OSE and SP) rely on phase-folded information, so that the individual TTVs, TDVs and flux loss of the transits is lost. On the positive side, time-dependent red noise should also be reduced in the folding process. A competing search strategy, as employed by Kipping et al. (2014b), avoids transit folding but instead uses a photodynamical approach and brute-force calculates and fits all possible configurations. Such a search is beyond the scope of this paper, but could ultimately be used to (in)validate promising results from OSE and SP. As the photodynamical method is computationally expensive, OSE+SP can deliver candidates for further investigation.

For the super-stack of all suitable planets of $35d < P < 80d$, we find an average flux loss of $6 \pm 2 \times 10^{-6}$ (6ppm), corresponding to an average total exomoon radius of about the size of Ganymede when transiting a sun-like star. The OSE is insensitive to longer-period planets with four years of *Kepler* data, but there is a hint of less moon signal in planets with $P < 35d$.

At first glance, the high moon radii of the individual candidates seem implausible, as there is no such large moon in our own solar system. However, our solar system might not be the norm – we have no Hot Jupiters, warm Neptunes, or Super-Earths in our solar system, and thus no reference for typical moons around such planets. Also, there is a strong selection bias, based on the detection limits (section 4.4), and in addition the simple fact that the strongest dips are most significant. The first moons to be found will likely be at the long (large/massive) end of exomoon distribution, as was the case for exoplanets.

If all candidates shown in this work turn out to be noise only, then the result of this paper is that the OSE, in its current state and with current data, is of little use for the detection of exomoons. On the other hand, confirmation of any one candidate would make it an immensely useful method. Even a single exomoon confirmation would be a landmark in exoplanet science, and establish $\eta_{\leftmoon} > 0$. As such, the potential moons discussed in this paper should be only as *candidates* worth further investigation.

ACKNOWLEDGEMENTS

We thank René Heller, Andrew Howard, Robert Szabó, Gyula Szabó and Attila Simon for their feedback on an earlier draft, which increased the quality of this paper. We also thank David Kipping for pointing out several weaknesses of the OSE method.

[4] Johann Wolfgang von Goethe (1749 - 1832).

REFERENCES

Awiphan, S., Kerins, E. 2013, MNRAS, 432, 2549
Barnes, J. W., Fortney, J, J. 2004, ApJ, 616, 1193-1203
Barnes, J. W., O'Brien, D. P. 2002, ApJ, 575, 1087
Burke, C. J., Bryson, S. T., Mullally, F. et al. 2014, ApJS, 210, 2, 19
Caldwell, D. A., Kolodziejczak, J. J., Van Cleve, J. E. et al. 2010, ApJ, 713, L92-L96
Canup, R. M., Ward, W. R. 2006, Nature, 441, 834-839
Carter, J. A., Agol, E., Chaplin, W. J. et al. 2012, Science, 337, 6094
Cassidy, T. A., Mendez, R., Arras, P. et al. 2009, ApJ, 704, 2
Said, S., Dickey, D. 1984, Biometrika, 71, 3, 599-607
Domingos, R. C., Winter, O. C., Yokoyama, T. 2006, MNRAS, 373, 3
Dougherty, M. K., Esposito, L. W., Krimigis, S. M. 2009, Saturn from Cassini-Huygens, Springer Science+Business Media B.V.
Forgan, D., Yotov, V. 2014, MNRAS, 441, 4
Gandolfi, D., Parviainen, H., Deeg, H. J. et al. 2015, A&A, in press, arXiv: 1409.8245
Gautier, T. N., Charbonneau, D., Rowe, J. F. et al. 2012, ApJ, 749, 1, 15
Gilliland, R. L., Jenkins, J. M., Borucki, W. J. et al. 2010, ApJ, 713, 2, L160-L163
Heller R. 2014, ApJ, 787, 14
Heller, R., Williams, D., Kipping, D. M. et al. 2014, Astrobiology, 14, 9
Hinkel, N. R., Kane, S. R. 2013, ApJ, 774, 1, 27
Kipping, D. M. 2011, MNRAS, 416, 1
Kipping, D. M., Fossey, S. J., Campanella, G. 2009, MNRAS, 400, 1, 398-405
Kipping, D. M., Hartman, J., Buchhave, L. A. et al. 2013, ApJ, 770, 2, 101
Kipping, D. M., Forgan, D., Hartman, J. et al. 2013, ApJ, 777, 2, 134
Kipping, D. M., Huang, C., Nesvorný, D. et al. 2014, ApJ, in press, arXiv: 1411.7028
Kipping, D. M., Nesvorný, D., Buchhave, L. A. et al. 2014, ApJ, 784, 1, 28
Kipping, D. M., Huang, C., Torres, G. et al. 2015, American Astronomical Society, AAS Meeting 225, 420.08
Lissauer, J. J., Jontof-Hutter, D., Rowe, J. F. et al. 2013, ApJ, 770, 131
Marcy, G. W., Isaacson, H., Howard, A. W. 2014, ApJS, 210, 2, 20
Mayor, M., Queloz, D. 1995, Nature, 378, 6555, 355-359
Nesvorný, D., Kipping, D. M., Terrell, D. et al. 2013, ApJ, 777, 1, 3
Porter, S. B., Grundy, W. M. 2011, ApJ, 736, L14-L20
Rasio, F. A., Tout, C. A., Lubow, S. H. et al. 1996, ApJ, 470, 1187
Rowe, J. F., Bryson, S. T., Marcy, G. W. 2014, ApJ, 784, 1, 45
Rowe, J. F., Coughlin, J. L.; Antoci, V. 2015, ApJS, in press, arXiv: 1501.07286
Santerne, A., Hébrard, G., Deleuil, M. 2014, A&A, 571, A37
Sato, M., Asada, H. 2009, PASJ, 61, 4
Sato, M., Asada, H. 2010, PASJ, 62, 5
Simon, A. E., Szabó, Gy. M., Kiss, L. L. et al. 2012, MNRAS, 419, 1
Smith, J. C., Stumpe, M. C., Van Cleve J.E. et al. 2012, PASP, 124, 919
Tal-Or, L., Mazeh, T., Alonso, R. et al. 2013, A&A, 553, A30
Weidner, C., Horne, K. 2010, A&A, 521, A76
Williams, D. M. 2013, Astrobiology, 13, 315-323
Wright, J. T., Fakhouri, O., Marcy, G. W. et al. 2011, PASP, 123, 902